UNIVERSITÉ DU QUÉBEC À MONTRÉAL

ON THE INTEGRATION OF CHROMOPHORES WITH MULTIDIRECTIONAL CHARGE-TRANSFER WITH SILICON WAVEGUIDES FOR NONLINEAR APPLICATIONS

MASTER'S THESIS
PRESENTED
AS A PARTIAL REQUIREMENT
FOR THE MASTER'S DEGREE IN ELECTRICAL ENGINEERING

BY
MONIR DELAVARI

FEBRUARY 2016

UNIVERSITÉ DU QUÉBEC À MONTRÉAL

ÉTUDE SUR L'INTEGRATION DE CHROMOPHORES À TRANSFERT DE CHARGES MULTIDIRECTIONNEL AVEC DES GUIDES D'ONDE EN SILICIUM POUR DES APPLICATIONS NON-LINÉAIRES

MÉMOIRE
PRÉSENTÉ
COMME EXIGENCE PARTIELLE
DE LA MAÎTRISE EN GÉNIE ÉLECTRIQUE

PAR
MONIR DELAVARI

FÉVRIER 2016

TABLE OF CONTENTS

LIST OF FIGURES VI
LIST OF TABLES X
LIST OF ABBREVIATIONS XI
ABSTRACT XIV
RÉSUMÉ XV
CHAPTER I
THE RESEARCH PROBLEM 1
1.1 Optical Communication Systems 1
1.2 Silicon Photonics 3
1.3 Optical Slot Waveguides with Nonlinear Chromophores 5
1.4 Thesis Objectives 7
1.5 Thesis Outline 9
CHAPTER II
THEORETICAL BACKGROUNDG 11
2.1 Nonlinear Optics in Waveguides 11
2.1.1 Maxwell's Equations and Nonlinear Polarization 11
2.1.2 Optical Waveguides and Propagating Modes 13
2.1.3 Ideal Waveguide Mode Analysis 15
2.1.4 Modes in 3-D Waveguides 17
2.1.5 Beam Propagation Method (BPM) Technique 18
2.1.6 Third-order Nonlinear Interaction 20
2.2 Nonlinear Parameters 21
2.3 Couple-Mode Theory of Four-Wave Mixing 23
2.3.1 Origin of Four Wave Mixing 23
2.3.2 Coupled-Mode Theory 24
2.3.2.1 Wavelength Conversion 25
2.3.2.2 Chromatic Dispersion 26

2.4 Nonlinear Optical Slot Waveguides.....27
2.5 Multidirectional Charge-Transfer Transitions Molecules...32
2.5.1 Molecular Hyperpolarizability.....33
2.5.2 Third-Order Nonlinear Chromophores.....34

CHAPTER III

MATERIALS AND FABRICATION 35

3.1 Materials.....35
3.1.1 PMMA.....35
3.1.2 Crystal Violet.....36
3.2 Silicon Slot Waveguides.....37
3.2.1 Waveguide Design.....37
3.2.2 Device Fabrication.....42
3.2.3 Deposition of Crystal Violet.....45

CHAPTER IV

THIRD-ORDER NONLINEAR EFFECT IN SOI WAVEGUIDES 51

4.1 Numerical Calculations of Slot Waveguide Modes.....51
4.2 Effective Area of the Third-order Nonlinear Interaction....56
4.3 Dispersion and Phase-matching Condition.....58
4.4 Nonlinear Parameters of Crystal Violet.....60
4.4.1 Third Order Nonlinear Susceptibility.....60
4.4.2 Nonlinear Waveguide Parameter.....61
4.5 FWM-based Wavelength Conversion.....63

CHAPTER V

EXPERIMENTAL SETUP AND MEASURMENTS 67

5.1 Experimental Setup and Measurements.....67
5.1.1 Propagation Loss Measurements.....69
5.2 FWM-based Wavelength Conversion Experiment.....76
5.2.1 Experimental Setup for Four-wave mixing.....76

CHAPTER VI

CONCLUSION..... 79

REFERENCE.....83

LIST OF FIGURES

Figure 1.1: Two-photon absorption mechanism (adapted from (Paschotta, 2008)) **4**

Figure 1.2: Schematic of a slot waveguide using nonlinearities in the slot (From (Leuthold, Koos and Freude, 2010)) **6**

Figure 2.1: Basis structure of a slab waveguide (From (Okamoto, 2010)) **14**

Figure 2.2: The refractive indices of a strip waveguide. (From (Okamoto, 2010) **14**

Figure 2.3: Schematic of a slot waveguide using nonlinearities in the slot (From (Leuthold, Koos and Freude, 2010)) **17**

Figure 2.4: Schematic of a slot waveguide. The TE-mode (shown in orange) is confined in the low-index slot region [From (Anderson, Schmidt and Lipson, 2006)] **28**

Figure 2.5: Cross-section of waveguides a) Strip waveguide (core and cover nonlinearity) b) slot waveguide (cover nonlinearity) [From (Leuthold *et. al.*, 2009)] **29**

Figure 2.6: Molecular structure of p-nitroaniline with unidirectional charge transfer (("4-Nitroaniline ", n.d.)) **34**

Figure 3.1: Molecular structure of crystal violet [from (Greve *et. al.*, 1997)] 36

Figure 3.2: Calculated a)HOMO and b) LUMO for crystal violet[from (Greve *et. al.*, 1997)] 37

Figure 3.3: Top-view SEM picture of design. The letters refer to Table 3.1. 38

Figure 3.4: Slot waveguide structure.....40

Figure 3.5: Top-view SEM picture of the Y-branch 40

Figure 3.6: Top-view SEM picture of the coupler design used in sample.....41

Figure 3.7: Top-view SEM picture of grating coupler.....42

Figure 3.8: Image of the grating couplers at the end of one block of waveguides 42

Figure 3.9: Cross-section of SiPhotonics Standard Passives (PSV) FC and WG modules (Dumon, 2012) 43

Figure 3.10: Cross-section of SiPhotonics PSV with resist cladding (Dumon, 2012) 44

Figure 3.11: Sample covered with crystal violet 5 wt % dissolved in chlorobenzene 46

Figure 3.12: Sample covered with crystal violet 5 wt. % dissolved in chloroform 47

Figure 3.13: SEM picture of the cleaved sample deposited with 5 wt. % PMMA 48

Figure 3.14: SEM picture of the cleaved sample deposited with 1 wt. % crystal violet 48

Figure 4.1: Counter map of transverse index profile of a slot waveguide with crystal violet cladding. The colour scale represents the refractive index value .. 52

Figure 4.2: Top-view SEM picture of the slot waveguide..... 53

Figure 4.3: Normalized transverse E-field profile of the quasi-TE mode for n_{cover}=1.51 for a) w_s=100 nm b) w_s=120 nm c) w_s=130 nm d) w_s=140 nm. The color scale shows the electric field normalised amplitude. 54

Figure 4.4: Effective refractive index of crystal violet as a function of wavelength for for various slot widths 100 nm<w_s<140 nm 55

Figure 4.5: Horizontal cut of the E_x mode profile at Y=0 56

Figure 4.6: Effective area A_{eff} for various slot widths 100 nm<w_s<140 nm as a function of the cladding refractive index. 58

Figure 4.7: Simulated GVD for the TE mode as a function of wavelength for w_s=140 nm 59

Figure 4.8: Third order nonlinear susceptibility for a polymer film doped with 10 wt. % crystal violet as a function of wavelength (adapted from Ramos-Ortiz *et al.*, 2007) 61

Figure 4.9: Theoretical conversion efficiency as a function of idler wavelength for slot waveguides filled with crystal violet 10 wt. % for slot widths 100 nm< w_s< 140 nm 64

Figure 4.10: Theoretical conversion efficiency as a function of idler wavelength for a silicon channel waveguide 65

Figure 4.11: Theoretical conversion efficiency as a function of idler wavelength for slot waveguides with an input power of P_{in}=300 mW 66

Figure 4.12: Theoretical conversion efficiency as a function of idler wavelength for silicon waveguide with an input power of P_{in}=300 mW 66

Figure 5.1: Schematic of a grating coupler used to couple light into a photonic integrated circuit (adapted from (Pello, 2014)) 67

Figure 5.2: Loss measurement setup 68

Figure 5.3: Measurement of the insertion loss for the fundamental TE mode for slot waveguides with a slot width of w_s=140 nm and cladded with 5 wt% PMMA dissolved in chlorobenzene. 71

Figure 5.4: Expected conversion efficiency for slot waveguide with slot width of w_s= 140 nm filled with 1 wt. % crystal violet 75

Figure 5.5: FWM experimental setup: ECL: External cavity laser; EDFA: Erbium doped fiber amplifier; PC: Polarization controller; OSA: Optical spectrum analyzer; PM: Power meter (adapted from (Brès *et al.*, 2011)) 77

LIST OF TABLES

Table 2-1: Cladding nonlinearity for inorganic materials (adapted from (Koos *et. al.*, 2007)) **30**

Table 2-2: Cladding nonlinearity for organic materials (adapted from (Koos *et. al.*, 2007)) **31**

Table 3-1: Waveguides' dimensions **39**

Table 3-2: Overview of process modules **44**

Table 4-1: Effective refractive index of crystal violet for different slot width **55**

Table 4-2: Summary of material parameters and nonlinear coefficients for crystal violet **62**

Table 4-3: Nonlinear parameter and nonlinear effective area for different slot widths **62**

Table 5-1: Measurements of insertion losses, propagation losses and coupling losses for waveguides filled with PMMA 5 wt. % dissolved in chlorobenzene **72**

Table 5-2: Measurements of insertion losses, propagation losses and coupling losses for waveguides filled with PMMA 5 wt. % dissolved in chloroform **73**

Table 5-3: Measurements of insertion losses, propagation losses and coupling losses for waveguides filled with crystal violet 1 wt. % dissolved in chloroform **74**

LIST OF ABBREVIATIONS

A_{eff}	Effective modal area
CT	Charge transfer
CV	tris(4-N N-dimethylamino phenyl)methyl (Crystal violet)
CW	Continuous wave
BPM	Beam Propagation Method
DANS	4-dialkyamino-4'nitro-stilbene
DFWM	Degenerate four-wave mixing
DI	De-ionized
D_{inter}	Interaction domain
DUV	deep ultraviolet
ECL	External cavity laser
EDFA	Erbium-doped fiber amplifier
FC	Fiber coupler
FCA	Free-carrier absorption
FDTD	Finite-difference Time-domain
FEFD	Finite Element Frequency Domain

FWM	Four-wave mixing
GVD	Group velocity dispersion
HOMO	Highest occupied molecular orbital
IR	Infrared
LOMO	Lowest unoccupied molecular orbital
mW	Milliwatt
n_{eff}	Effective refractive index
OSA	Optical spectrum analyser
PC	Polarization controller
PC-CT	periphery-to-center charge-transfer
PDA	Polydiacetylene
PMMA	Poly (methyl methacrylate)
PSV	Passive
PTA	polytriactelyene
PTS	poly(p-toluene sulphonate)
RESCLAD	Resist cladding
SEM	Scanning electron microscopy
Si	Silicon
SiO_2	Silicon dioxide
SOI	Silicon on insulator
SPM	Self-phase modulation

Tbs^{-1}	Terabit per second
TE	Transverse electric
TEE	tetraethynylethene
TM	Transverse magnetic
TIR	Total internal reflection
TPA	Two-photon absorption
WG	Waveguide
XPM	Cross phase modulation

ABSTRACT

SOI-based nonlinear slot waveguides cladded with crystal violet are of great interest for ultrafast all-optical signal processing. In this work, the optical properties of slot waveguides filled with crystal violet were investigated experimentally and their nonlinear potential was studied numerically.

This thesis covers the theoretical basics of nonlinear optics, slot waveguide design, device fabrication, a simulation study of the four-wave mixing conversion efficiency in slot waveguides filled with crystal violet, the challenges of using crystal violet in the cladding of silicon photonic devices, a deposition process for crystal violet chromophores in a PMMA host on silicon slot waveguides, and experimental demonstrations and characterisation of the propagation losses of slot waveguides filled with a polymer containing crystal violet chromophores.

The dispersion profile, the effective mode area and the nonlinear parameters of slot waveguides were estimated by using a MATLAB script. The slot waveguide geometry and design were optimized to give an effective core area of 0.321 μm^2, leading to a nonlinear coefficient of 394 $(Wm)^{-1}$for a slot width of 140 nm for the fundamental TE mode. A combination of standard photolithography and etching was used to fabricate the waveguides with the desired dimensions. The linear characterization of these slot waveguides cladded with crystal violet shows that the lowest linear loss achieved to date is approximately 11 dB/cm.

This study prepared the foundation for the development of a novel category of highly nonlinear hybrid silicon devices that exploit the unique design and optimization opportunities made possible by chromophores relying on multi-charge transfer transitions.

Keywords: Slot-waveguides, Nonlinear chromophore, Third order Nonlinear effect, Conversion efficiency

RÉSUMÉ

Les guides d'onde à rainure non linéaire ayant une gaine contenant du cristal violet sont d'un grand intérêt pour le traitement tout-optique ultra-rapide de signaux lumineux. Dans ce mémoire, les propriétés optiques de guides d'onde à rainure remplis avec du cristal violet ont été étudiées expérimentalement et leur potentiel non linéaire a été étudié numériquement.

Ce mémoire couvre les bases théoriques de l'optique non linéaire, la conception de guide d'ondes à rainure, leur fabrication, une étude par simulation de l'efficacité du mélange à quatre ondes dans des guides d'onde à rainure remplies de cristal violet, les défis de l'utilisation du cristal violet dans la gaine de dispositifs photoniques en silicium, un procédé de dépôt pour les chromophores de cristal violet dans un hôte de PMMA sur des guides d'onde à rainure en silicium et des démonstrations expérimentales et la caractérisation des pertes de propagation des guides d'ondes à rainure remplis d'un polymère contenant des chromophores de cristal violet.

La dispersion, la surface effective du mode et les paramètres non linéaires des guides d'ondes à rainure ont été estimés en utilisant un script de simulation fonctionnant avec MATLAB. La géométrie des guides d'onde à rainure a été optimisée pour obtenir une surface effective de 0,321 um^2, ce qui produit un coefficient non linéaire de 394 $(Wm)^{-1}$pour une largeur de rainure de 140 nm pour le mode TE fondamental. Une combinaison de photolithographie et de gravure sèche a été utilisée pour fabriquer des guides d'onde avec les dimensions désirées. La caractérisation de ces guides d'onde à rainure ayant une gaine de cristal violet montre que la plus faible perte linéaire réalisée à ce jour avec ce type de guide d'onde est d'environ 11 dB / cm.

Cette étude a jeté les bases pour le développement d'une nouvelle catégorie de dispositifs hybrides fortement non linéaires qui exploitent les possibilités de conception et d'optimisation uniques des chromophores possédant plusieurs transitions de transfert de charge.

Mot de clés : Guides d'onde à rainure, Chromophore non linéaire, Effet non linéaire du troisième ordre, Efficacité de conversion

CHAPTER I

THE RESEARCH PROBLEM

Over the past few years, highly nonlinear silicon waveguides have been developed in order to increase the flexibility of optical networks. They achieve this by enabling all-optical processing, which can handle enormous bandwidth and can be transparent to modulation formats. Silicon nanowaveguides have been optimized to enhance nonlinear effects such as four-wave mixing (FWM). Furthermore, they have demonstrated great potential for wavelength conversion (Ophir *et. al.*, 2012; Xu *et. al.*, 2011). However, there are important limitations to the conversion efficiency that can be achieved with silicon waveguides, such as the losses caused by two-photon absorption at telecommunication bandwidths, or the significant input power (>100mW) that must be coupled into them to observe nonlinear effects. Thus, ways to reduce the impact of these limitations must be investigated to be able to perform all-optical signal processing by taking advantage of ultrafast $\chi^{(3)}$-nonlinearities and the large optical bandwidth of silicon waveguides.

In this chapter, the growth of the optical communication field is discussed, and the potential of integrated silicon photonics as a solution to overcome the challenges posed by high data rates is presented. Finally, the objectives and the organization of this thesis are described.

1.1 Optical Communication Systems

Recently, optical communication systems have gathered a lot of attention and tremendous work has been done, especially to increase their transmission rate. Moreover, the large bandwidth available in optical fibers can be used to create optical links with transmission rates of more than 1 Tbs^{-1} on a single fiber by using

wavelength division multiplexing and these signals can be sent across hundreds of kilometers.

Furthermore, the continuation of Moore's law (Moore, 1998), which states that the number of transistors on an electronic integrated circuit should double every two years, has caused an exponential increase in computing power. As a result, transmission systems with large bandwidth are required to transport and utilize the tremendous amounts of data that is produced. Accordingly, advancements in the fields of optics and microfabrication have enabled the development of a vast number of integrated optical devices that make possible the creation of high capacity data links. Hence, integrated optic plays a crucial role in the optical fiber networks that form the backbone of the Internet (Levy, 2011).

The demand for higher data rates and reduced power consumption means that optics hold distinct advantages over electronics (Preston, 2011). For example, in electrical connections the signal attenuation with distance is very high (Gambling, 2000) but optical networks can provide significantly larger bandwidth, lower power consumption per bits and have practically no distance limitations. However, the cost of optical transceivers has always been an issue but this could be overcome thanks to integrated photonic devices that can be fabricated cheaply by taking advantages of the new developments and techniques in microfabrication processes (Paniccia, Krutul et. Koehl, 2004). Also, to build optical systems, the alignment of the optical components must be done accurately, which requires sophisticated packaging techniques. The development of advanced optical networks and the replacement of large optical sub-systems by chip-scale devices make the improvement of integrated photonics crucial. Since ultrafast nonlinear optical effects can be employed to process signals at frequencies exceeding the THz, all-optical signal processing has the potential to enable photonic devices operating at Tbit/s line rates (Igarashi et Kikuchi, 2008; Willner et al., 2011). Moreover, because telecommunication networks rely more and more on optical signals, an effective and low-cost technology is needed to build all-optical signal processing components that can ensure that system speed and capacity

continue to increase. Thus, the increasing demand for high-speed and reconfigurable optical networks requires the study of optical signal processing. Integrated photonics can perform all-optical data signal processing at decreased costs. For instance, FWM is a nonlinear effect that has proven useful to create all-optical signal processing components, such as wavelength conversion devices (Lin *et. al.*, 2006) that could be used to resolve contention problems.

1.2 Silicon Photonics

Various low-index-contrast material systems, such as doped silicon dioxide (SiO_2) and polymers (Foresi *et. al.*, 1997 ; Kuwata-Gonokami *et. al.*, 1995 ; Little *et. al.*, 2004), have been used to fabricate optical waveguides and integrated photonic devices over the past decade. However, lately high-index-contrast material systems, such as silicon (Si) and III-V compounds (Masanovic *et. al.*, 2005; Soltani, Yegnanarayanan et. Adibi, 2007 ; Vlasov *et. al.*, 2005), have gained more attention because they can provide high optical confinement, which make possible high levels of integration and can increase optical power densities. Among high-index-contrast material platforms, silicon-on-insulator (SOI) is the most used for photonic applications because of its cost advantages and of the advanced fabrication processes that are commercially available.

Silicon photonics has been a rapidly growing field of research because of the increasing accessibility of high-quality silicon-on-insulator (SOI) wafers (Celler and Cristoloveanu, 2003) where a layer of silicon oxide separates a layer of single-crystal silicon from the bulk handle wafer. Important functionalities were demonstrated on this platform. For example, many important components can be fabricated on a silicon photonic chip such as: photodetectors (Assefa, Xia and Vlasov, 2010; Kang *et. al.*, 2009), hybrid laser sources (Fang *et. al.*, 2006), filters (Dong *et. al.*, 2010; Xia *et. al.*, 2007) and modulators (Reed *et. al.*, 2010). Thus, silicon photonics has enabled the integration of numerous components on a single chip.

By using silicon, which has a high refractive index (n≈3.48) at telecommunication wavelength (λ=1550 nm), it is possible to obtain a strong confinement of the optical modes. Silicon possess a high nonlinear refractive index, n_2, in the range of $(4\text{-}9)\times10^{-14}$ cm^2W^{-1} (Dinu, Quochi and Garcia, 2003 ; Fukuda *et. al.*, 2005 ; Tsang *et. al.*, 2002), which is three orders of magnitude larger than silica glass. Moreover, the tight modal confinement in SOI waveguides has a great impact on the nonlinear parameter since it is inversely proportional to the effective area of the mode, $\gamma \propto n_2/A_{eff}$ (Foster *et. al.*, 2006). Although silicon has been the core material used in the microelectronics industry due to its versatility and cost, it has some important drawbacks for nonlinear optics. For example, its energy gap is 1.12eV, and thus, at telecommunication wavelengths two-photon absorption appears because the bandgap is less that the energy of two photons at these wavelengths. Furthermore, two-photon absorption (TPA) induces losses that are compounded by the carriers generated, which produce free carrier absorption (FCA). In the TPA process (see Fig. 1.1) an electron makes a transition from the valence band to the conduction band of silicon by the simultaneous absorption of two laser photons, which increases the concentration of free charges. Therefore, the combination of TPA and FCA limits the efficiency of nonlinear processes at telecommunication wavelengths in silicon

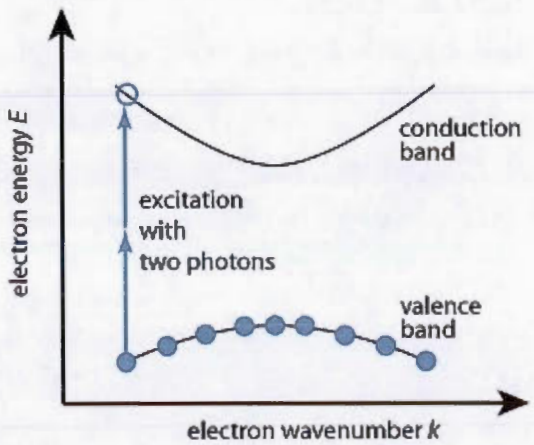

Figure 1.1: Two-photon absorption mechanism (adapted from (Paschotta, 2008))

More generally, the causes behind the challenges of using silicon in integrated optics are as follows: (1) the indirect minimum-energy bandgap, which leads to inefficient stimulated emission and impractical laser action; (2) the centrosymmetry of silicon crystal, which limits the electro-optic effects used for active devices such as modulators; and (3) at telecommunication wavelengths, silicon has a large two-photon absorption coefficient that affects the third-order nonlinear effects (Leuthold, Koos et. Freude, 2010). For these reasons, it is desirable to use more efficient materials and combine them with a silicon structure for certain on-chip functions. This is the motivation behind the work presented in this thesis, which investigates the development of novel hybrid silicon waveguides that could enable nonlinear applications.

1.3 Optical Slot Waveguides with Nonlinear Chromophores

As mentioned in the previous section, despite the obvious advantages of using silicon to build devices for optical telecommunication systems, it has severe limitations for a few functionalities, in particular those relying on nonlinear effects. Moreover, its high refractive index makes it difficult to couple light efficiently to cladding materials because of the high confinement it provides. Nevertheless, it is possible to achieve a very high level of interaction with a cladding material by using a 'slot waveguide' structure. One can then work with a highly nonlinear cladding material with low two-photon absorption and benefit from a high level of optical confinement in the slot region.

The silicon slot waveguide structure was developed to generate an intense optical mode in the low index region of the waveguide (see Fig 1.2). This structure is made of two channel waveguides with a high refractive index core material that are brought

in close proximity to form a narrow low index slot region in which most of the optical power will be confined (Almeida *et. al.*, 2004).

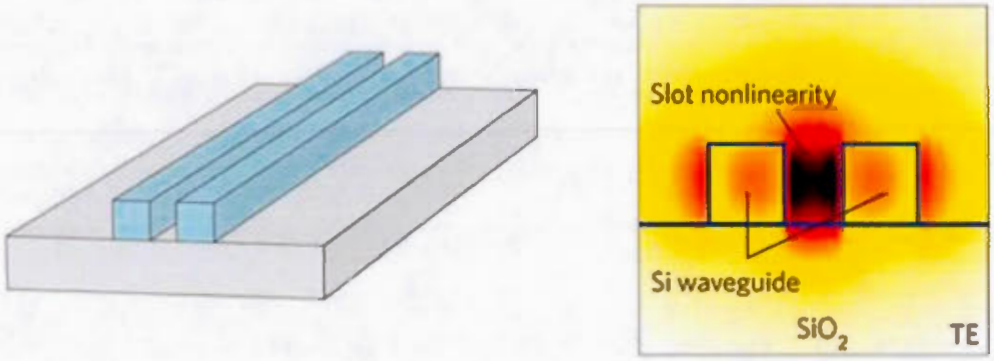

Figure 1.2: Schematic of a slot waveguide using nonlinearities in the slot (From (Leuthold, Koos and Freude, 2010))

The slot waveguide structure functions as a result of the electric field discontinuity at the high-index contrast barrier between the silicon core and the cladding. As a result, the electric field is more intense in the slot region than in the silicon waveguides. Furthermore, the slot waveguides can be used for various functionalities, such as light emission, electro optic modulators (Baehr-Jones *et. al.*, 2008), amplification, and waveguides with ultrafast nonlinearity and supressed free-carrier effects (Koos *et. al.*, 2009) because of the strong electric field enhancement in the slot region and that this slot can be filled with a variety of low-index materials (Almeida *et. al.*, 2004; Xu *et. al.*, 2004).

To fill the low-index slot region, the nonlinear optical chromophore tris(4-N,N-dimethylaminophenyl)methyl (also known as 'crystal violet') which has a high second-order hyperpolarizability γ and display multi-charge transfer transitions, was chosen for this study. It was demonstrated experimentally that the high second-order hyperpolarizability, γ, provided by the molecular structure of crystal violet within the range of wavelengths used in optical telecommunication originates from the conjugated and highly polarized π-electron backbone (Bosshard *et. al.*, 1996 ; Greve *et. al.*, 1997). Thus, octupolar chromophores with three-fold symmetry and multi-

charge transfer transitions, such as crystal violet, provide higher hyperpolarizability and they show multiple donor-acceptor substituents due to the chromophore units, polymer backbone, and their molecular symmetry that helps to have a multidirectional charge transfer.

Silicon slot waveguides with a nonlinear cladding material have demonstrated a small effective mode area (A_{eff}) and a high nonlinear parameter (γ) that make them suitable to build wavelength converters with high conversion efficiency (Liu *et. al.*, 2011). In FWM-based wavelength conversion, the conversion bandwidth and the efficiency are closely related to the phase-matching condition, which can be optimized by engineering the dispersion profile of the waveguides (Gao, Li and Zhang, 2010). In this work, for the first time, crystal violet, which displays periphery-to-center charge-transfer transitions, is used as the cladding material in slot waveguide structures. We analyze the nonlinear parameters of slot waveguides filled with crystal violet as a function of their geometry, which impacts the effective mode area and the waveguide dispersion profile. Based on the optimized slot waveguide configuration, the FWM conversion efficiency has been studied numerically. Furthermore, the integration challenges of polymers containing crystal violet molecules with silicon slot waveguides were investigated experimentally.

1.4 Thesis Objectives

Various nonlinear polymers have been used as cladding material to fill slot waveguides (Koos *et. al.*, 2009). However, nonlinear chromophores, such as crystal violet, with a molecular arrangement that enables multidirectional charge-transfer transitions can be optimized with a unique method demonstrated by Greve *et. al.* (1997). Therefore, this type of chromophore could potentially be used to realize innovative and high performance devices.

In this work, the integration of this highly nonlinear chromophore with silicon waveguides having a slot geometry is studied for the first time. The contributions achieved in thesis are intended to provide an initial study of the optical properties of slot waveguides filled with crystal violet and their nonlinear potential. SOI-based nonlinear slot waveguides cladded with crystal violet could be of great interest for ultrafast all-optical signal processing. This investigation of hybrid silicon waveguides cladded with crystal violet chromophores that lead to the following contributions:

- The first simulation study of the four-wave mixing conversion efficiency in slot waveguides filled with crystal violet;
- The first experimental characterisation of the propagation losses of slot waveguides filled with PMMA diluted in chloroform;
- The first deposition process for crystal violet chromophores in a PMMA host on silicon slot waveguides;
- The first study on the challenges of using crystal violet in the cladding of silicon photonic devices;
- The first experimental demonstration and characterisation of the propagation losses of slot waveguides filled with a polymer containing crystal violet chromophores.

The goal of this work is to lay the foundation for the development of a novel category of highly nonlinear hybrid silicon devices that exploit the unique design and optimization opportunities made possible by chromophores relying on multi-charge transfer transitions.

This thesis could not have been completed without collaboration of Dr. Mohammed Rahim for design of the slot waveguides, CMC Microsystems and IMEC for fabrication of the samples, Danny Chhin for preparation of the crystal violet solutions and the training offered by Dr. Hadi Rabbani for the characterisation. My main tasks during this project were to perform the simulations, develop the deposition

recipe to make possible the integration of the chromophores on the silicon waveguides, and to carry out the experimental loss measurements.

1.5 Thesis Outline

This thesis is organized in the following manner. Chapter 2 gives a brief theoretical background on nonlinear optical waveguides. The fundamental electromagnetic theory is described to understand the nonlinear phenomena in integrated optical waveguides and Maxwell's equations with nonlinear polarization are reviewed. Nonlinear optical parameters are then presented and the coupled mode theory of FWM is explained with coupled differential equations. The structure of optical slot waveguides is shown and finally molecules with multidirectional charge-transfer transitions, which are used as the interaction material filling in the slot waveguides, are introduced. Chapter 3 describes specifically the nonlinear material used for filling the slot waveguides, the device structure and design, and the fabrication processes that were used for this work. Chapter 4 discusses the theoretical and simulation studies on slot waveguides with crystal violet such as their mode profile, effective mode area, nonlinear parameter, dispersion profile, and FWM conversion efficiency. Finally, chapter 5 presents the experimental results of the propagation and insertion loss measurements of slot waveguides filled with crystal violet.

CHAPTER II

THEORETICAL BACKGROUND

To describe nonlinear optical phenomena in integrated optical waveguides, a fundamental introduction to basic electromagnetic theory is necessary. The formalisms presented here are based on basic knowledge of electromagnetics and nonlinear optical phenomena, which various books discuss in details (Agrawal, 2013; Boyd, 2008 ; Shen, 1984). The Maxwell's equations are presented and we show that the polarization field, which is related to the strength of the electric field, has higher order terms that leads to nonlinearities such as the four-wave mixing (FWM) process. Following this, we describe the optical susceptibility when multiple fields are presented. The parameters influencing nonlinear effects are discussed and the coupled mode theory of FWM is presented. Light confinement in slot waveguides is explained. Lastly, optical chromophores with multidirectional charge transfer transitions are discussed.

2.1 Nonlinear Optics in Waveguides

2.1.1 Maxwell's Equations and Nonlinear Polarization

Maxwell's equations can be used to explain the propagation of optical fields in waveguides.If we consider the macroscopic case where no free carriers and currents are present, then Maxwell's equations take the following form (Diament, 1990):

$$\nabla \times \mathbf{E} = -\frac{\partial \mathbf{B}}{\partial t}, \tag{2.1}$$

$$\nabla \times \mathbf{H} = \boldsymbol{J} + \frac{\partial \mathbf{D}}{\partial t}, \tag{2.2}$$

$$\nabla . \boldsymbol{D} = \rho_f, \tag{2.3}$$

$$\nabla . \mathbf{B} = 0, \tag{2.4}$$

where **E** is the electric field vector, **H** is the magnetic field vector, **D** is the electric flux density and **B** is the magnetic flux density which is related to the magnetic field **H** by

$$\mathbf{B} = \mu_0 \mathbf{H} + \mathbf{M}, \tag{2.5}$$

where $\mu_0 = 1.25664 \times 10^{-6}$ V s /(A m) is the magnetic permeability of vacuum, and **M** is the induced magnetic polarization. A three-dimensional space is considered and the vector $\mathbf{r}=(x, y, x)$ is a point in this space.

For a medium where there are no free charges, the current density, **J**, and the charge density, ρ_f, are 0; furthermore for optical waveguides in a nonmagnetic medium **M**=0.

The relation between the electric field **E** and the electric displacement **D** is:

$$\boldsymbol{D} = \epsilon_0 \mathbf{E} + \mathbf{P}, \tag{2.6}$$

where $\epsilon_0 = 8.85419 \times 10^{-6}$ A s /(V m) is the electric permittivity of vacuum, and **P** is the induced electric polarization.

The polarization can be expressed as a power series of the electric field amplitude for nonlinear optics (Boyd, 2008)

$$\boldsymbol{P}(\boldsymbol{r}, t) = \epsilon_0 [\chi^{(1)} \mathbf{E}(\boldsymbol{r}, t) + \chi^{(2)} \mathbf{E}(\boldsymbol{r}, t)^2 + \chi^{(3)} \mathbf{E}(\boldsymbol{r}, t)^3 + \cdots] \tag{2.7}$$

where $\chi^{(j)}$ is the i^{th} order susceptibility. The dominant contribution to **P** is shown by $\chi^{(1)}$. The second order susceptibility, $\chi^{(2)}$, in isotropic medium is zero. Thus $\chi^{(3)}$ becomes the lowest nonlinear term of the polarization which is the third-order susceptibility (Boyd, 2008 ; Shen, 1984).

In nonlinear optics if we consider only the third-order nonlinear effects controlled by $\chi^{(3)}$ (Boyd, 2008), the polarization can be expressed in two parts as

$$\boldsymbol{P}(\boldsymbol{r}, t) = \boldsymbol{P}^{(lin)}(\boldsymbol{r}, t) + \boldsymbol{P}^{(nl)}(\boldsymbol{r}, t), \tag{2.8}$$

where $\boldsymbol{P}^{(lin)}$and $\boldsymbol{P}^{(nl)}$are the linear and nonlinear parts that are related to the electric field by the following equations (Boyd, 2003, 2008 ; Shen, 1984)

$$\boldsymbol{P}^{(lin)}(\boldsymbol{r},t) = \epsilon_0 \int_{-\infty}^{+\infty} \chi^{(1)}(t-t').\mathbf{E}(\boldsymbol{r},t')\,dt', \tag{2.9}$$

$$\begin{aligned} \boldsymbol{P}^{(nl)}(\boldsymbol{r},t) = \epsilon_0 \int_{-\infty}^{t} dt_1 \int_{-\infty}^{t} dt_2 \int_{-\infty}^{t} dt_3 \\ \times \chi^{(3)}(t-t_1, t-t_2, t-t_3) \\ \vdots \mathbf{E}(\boldsymbol{r},t_1)\mathbf{E}(\boldsymbol{r},t_2)\mathbf{E}(\boldsymbol{r},t_3). \end{aligned} \tag{2.10}$$

Eq. (2.10) provides a good understanding of the general form of the origin of third-order nonlinear effects. In addition $\boldsymbol{P}^{(nl)}$, the nonlinear polarization, in Eq. (2.8) is much weaker than the linear polarization, therefore $\boldsymbol{P}^{(nl)}$ can be considered as a small perturbation to the induced polarization.

2.1.2 Optical Waveguides and Propagating Modes

The design of integrated optical circuits requires the creation of optical waveguides. Thus, to put into context the work explained later in this thesis, an introduction to waveguide modes is presented. First, an ideal simple one dimensional optical waveguide (i.e. a slab waveguide) (see fig 2.1) is described to provide a basic understanding of how optical waveguides function and then the waveguide modes are derived using Maxwell's equations.

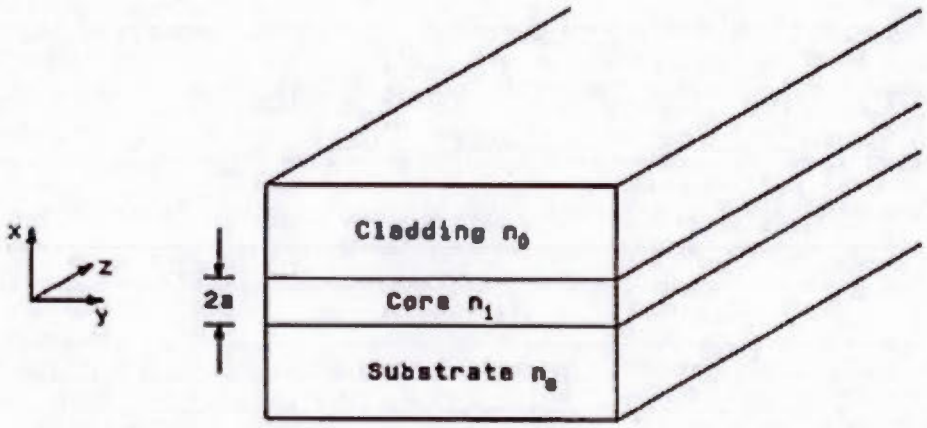

Figure 2.1: Basis structure of a slab waveguide (From (Okamoto, 2010))

An optical waveguide has a core, a cladding and a substrate and it is uniform in at least one direction and able to direct light along an axis (see Fig. 2.1). The refractive index of the cladding n_0 must be lower than that of the core n_1. The principle confining the light beam into the waveguide structure can be understood as total internal reflection (TIR), which can be derived using Snell's law.

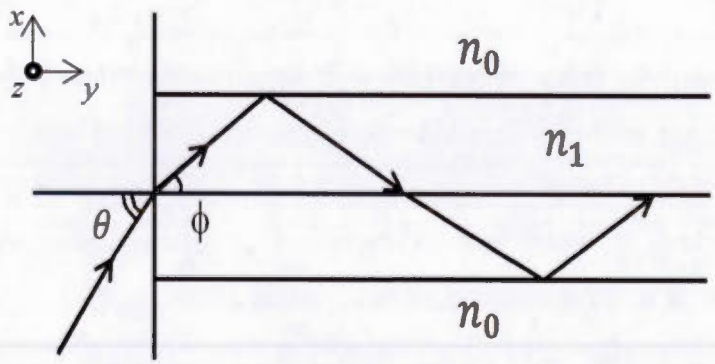

Figure 2.2: The refractive indices of a strip waveguide. (From (Okamoto, 2010)

For TIR, the following condition must be satisfied at the core-cladding interface (Okamoto, 2010):

$$n_1 \sin(\pi/2 - \phi) \geq n_0, \tag{2.11}$$

The relation between the incident angle θ and ϕ can be shown as:

$$\sin\theta = n_1 \sin(\phi) \leq \sqrt{{n_1}^2 - {n_0}^2}, \tag{2.12}$$

Hence, the critical condition for TIR is

$$\theta = \sin^{-1}\sqrt{{n_1}^2 - {n_0}^2} \equiv \theta_{max}, \tag{2.13}$$

A plane wave propagating along the z-direction has phase fronts perpendicular to the light rays. The wavenumber and wavelength of light in the core are kn_1 and λ/n_1, respectively, where $k = 2\pi/\lambda$ and λ is the wavelength of light in vacuum. The propagation constants along y and x are given by (Okamoto, 2010):

$$\begin{aligned} \beta &= kn_1 \cos\phi \\ \kappa &= kn_1 \sin\phi \end{aligned} \tag{2.14}$$

In order to obtain a guided mode, the condition for constructive interference must be satisfied and is given by the relation:

$$\tan(kn_1 \sin\phi - \frac{m\pi}{2}) = \sqrt{\frac{2\Delta}{sin^2\phi} - 1}. \tag{2.15}$$

where m is integer. Equation (2.15) shows that the propagation angle of the light ray is discrete and is determined by the waveguide structure (core radius a, refractive index n_1, refractive index difference Δ). The optical field distribution that satisfies the phase-matching condition of Eq. (2.15) is called the mode.

2.1.3 Ideal Waveguide Mode Analysis

In integrated photonic circuits the waveguides usually support only a single mode (Radamson et Thylen, 2014). Hence modal analysis is an important aspect in the design process since it provides information on the modes that propagate, their shapes and their propagation constants (Scarmozzino *et. al.*, 2000). In this section, the propagation characteristics of an ideal slab waveguide (see Fig. 2.1), which were explained based on simple ray tracing in section 2.1.2, are derived rigorously using wave analysis.

Maxwell's Eq. (2.1) and (2.2) in the frequency domain become two coupled differential equations for electric and magnetic fields:

$$\nabla \times \tilde{\mathbf{E}} = -\mu_0 \frac{\partial \tilde{\mathbf{H}}}{\partial t}, \tag{2.16}$$

$$\nabla \times \tilde{\mathbf{H}} = \epsilon_0 n^2 \frac{\partial \tilde{\mathbf{E}}}{\partial t}, \tag{2.17}$$

If we consider a uniform refractive index profile in the z-direction, we will have solutions in the following forms:

$$\tilde{\mathbf{H}} = \boldsymbol{H}(x,y)e^{i(\omega t-\beta z)}, \tag{2.18}$$

$$\tilde{\mathbf{E}} = \boldsymbol{E}(x,y)e^{i(\omega t-\beta z)}, \tag{2.19}$$

The propagation constant, β, is a function of the angular frequency ω, a positive (negative) value of $\beta(\omega)$ shows a propagation of the phase fronts in the positive (negative) z-direction.

For each electromagnetic field components if we replace Eq. (2.16) and (2.17) with Eq. (2.16) and (2.17), we have:

$$\begin{cases} \dfrac{\partial E_z}{\partial y} + i\beta E_y = -i\omega\mu_0 H_x \\ -\dfrac{\partial E_z}{\partial x} - i\beta E_x = -i\omega\mu_0 H_y \\ \dfrac{\partial E_y}{\partial x} - \dfrac{\partial E_x}{\partial y} = -i\omega\mu_0 H_z \end{cases} \tag{2.20}$$

$$\begin{cases} \dfrac{\partial H_z}{\partial y} + i\beta H_y = i\omega\epsilon_0 n^2 E_x \\ -\dfrac{\partial H_z}{\partial x} - i\beta H_x = i\omega\epsilon_0 n^2 E_y \\ \dfrac{\partial H_y}{\partial x} - \dfrac{\partial}{\partial y} = i\omega\epsilon_0 n^2 E_z. \end{cases} \tag{2.21}$$

In a slab waveguide, as shown in Fig. 2.1, **E** and **H** do not depend on the y-axis.

2.1.4 Modes in 3-D Waveguides

The electromagnetic field in strip waveguides (see Fig. 2.3) is concentrated in the core area and decays in the cladding region. The guided modes then split up into two different polarization subsets: a dominant E_x-component called (quasi-)TE- modes and a dominant E_y-component called (quasi-) TM-polarized modes.

Two independent set of electromagnetic modes exist in strip waveguides, the transverse electric (TE) and transverse magnetic (TM) modes, which are the electromagnetic field distributions when the electric (for TE modes) or the magnetic (for TM modes) field is situated in the plane and are perpendicular to the z-axis (Okamoto, 2010). Moreover, a finite number of guided modes and a continuous spectrum of radiation modes exist for a given waveguide at a fixed frequency ω and they form a complete set of Eigenmodes (Marcuse, 1972).

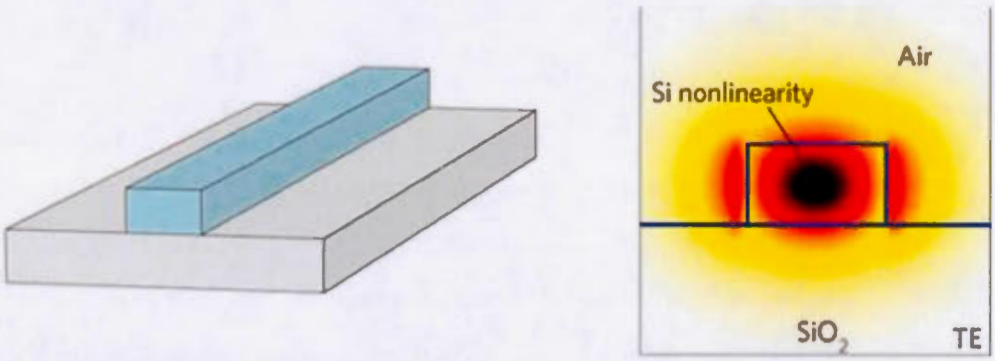

Figure II.3: Schematic of a slot waveguide using nonlinearities in the slot (From (Leuthold, Koos and Freude, 2010))

The wave equation for TE mode is represented by (Okamoto, 2010):

$$\frac{d^2E_y}{dx^2} + (k^2n^2 - \beta^2)E_y = 0, \tag{2.22}$$

where

$$H_x = -\frac{\beta}{\omega\mu_0}E_y, \tag{2.23}$$

$$H_z = \frac{i}{\omega\mu_0}\frac{dE_y}{dx}, \tag{2.24}$$

$$H_y = E_z = E_x = 0. \tag{2.25}$$

For TM mode, the wave equation is represented as:

$$\frac{d}{dx}\left(\frac{1}{n^2}\frac{dH_y}{dx}\right) + \left(k^2 - \frac{\beta^2}{n^2}\right)H_y = 0 \tag{2.26}$$

where

$$E_x = \frac{\beta}{\omega\epsilon_0 n^2}E_y, \tag{2.27}$$

$$H_z = -\frac{i}{\omega\epsilon_0 n^2}\frac{dH_y}{dx}, \tag{2.28}$$

$$H_z = H_x = E_y = 0. \tag{2.29}$$

There are several methods to calculate the mode profile of strip (also called channel) waveguides. The optical modes can be approximated with the effective index method or found more accurately with numerical methods.

Two popular numerical methods include: solving the two Maxwell curl equations in the frequency domain using Finite Difference in the Frequency Domain (FDTD) (Fallahkhair, Li et. Murphy, 2008); and another one is called the finite-difference Beam Propagation Method and it solves the scalar Helmholtz equations (Scarmozzino *et. al.*, 2000).

2.1.5 Beam Propagation Method (BPM) Technique

In this section the fundamental concept behind the Beam Propagation Method or BPM (Feit and. Fleck Jr, 1978 ; Scarmozzino *et. al.*, 2000) is described to find the optical modes of waveguides. BPM is a propagation technique for modeling light propagation in integrated and fiber optic photonic devices. It approximates the wave equation and solves the resulting equations numerically by using finite difference

methods as expressed in (Scarmozzino *et. al.*, 2000 ; Scarmozzino and Osgood Jr, 1991).

To solve the propagation problem, we need some basic knowledge about the refractive index distribution, $\boldsymbol{n}(x, y, z)$ and the input wave field $\boldsymbol{u}(x, y, z = 0)$. The algorithm requires additional numerical parameters including:

- A finite computational domain for x, y and z in the ranges (x_{min}, x_{max}), (y_{min}, y_{max}) and (z_{min}, z_{max}), respectively;
- The longitudinal step size, Δz;
- The transverse grid sizes, Δx and Δy.

By considering the scalar field, thus neglecting polarization effects, we can write the Helmholtz equation for monochromatic waves as:

$$\frac{\partial^2 \emptyset}{\partial x^2} + \frac{\partial^2 \emptyset}{\partial y^2} + \frac{\partial^2 \emptyset}{\partial z^2} + \boldsymbol{k}(x, y, z)^2 \emptyset = 0 \tag{2.30}$$

where the scalar electric field is $\boldsymbol{E} = \phi(x, y, z)e^{-i\omega t}$ and the spatially dependent wavenumber $\boldsymbol{k}(x, y, z) = k_0 \boldsymbol{n}(x, y, z)$ with $k_0 = 2\pi/\lambda$ being the wavenumber in free space.

In common guided-wave problems, there is a rapid phase variation in the direction of propagation, which follows the guiding axis. This quick change in the field ϕ can often be ignored since it occurs on a time scale much shorter than the changes due to modification in the device geometry. By introducing a slowly varying field $\boldsymbol{u}$, we can remove the rapid variation and simplify the problem:

$$\phi(x, y, z) = \boldsymbol{u}e^{i\bar{k}z} \tag{2.31}$$

where $\bar{k}$ is the reference wavenumber that represents the average phase variation of the field ϕ. If we substitute Eq. (2.31) into Eq. (2.30), we will have the following equation for the slowly varying field (Scarmozzino *et. al.*, 2000):

$$\frac{\partial^2 \mathbf{u}}{\partial z^2} + 2i\bar{k}\frac{\partial \mathbf{u}}{\partial z} + \frac{\partial^2 \mathbf{u}}{\partial x^2} + \frac{\partial^2 \mathbf{u}}{\partial y^2} + (k^2 - \bar{k}^2)\mathbf{u} = 0 \tag{2.32}$$

If we assume that the variation of $\boldsymbol{u}$ in the z-direction is slow, the first term in Eq. (2.32) can be neglected with respect to the second. The following equation is the basic BPM equation in three dimensions:

$$\frac{\partial \boldsymbol{u}}{\partial z} = \frac{i}{2\bar{k}}\left(\frac{\partial^2 \boldsymbol{u}}{\partial x^2} + \frac{\partial^2 \boldsymbol{u}}{\partial y^2} + (k^2 - \bar{k}^2)\boldsymbol{u}\right) \tag{2.33}$$

2.1.6 Third-order Nonlinear Interaction

In SOI based waveguides, the third-order nonlinear interaction can be realized by two methods. The first way is the Self-phase modulation (SPM)/Cross-phase modulation (XPM) caused by TPA and by the nonlinear interaction with the silicon waveguide core (Dulkeith *et. al.*, 2006; Tsang *et. al.*, 2002; Yamada *et. al.*, 2005). Otherwise, the silicon core can be imbedded in a nonlinear cladding material and, as a result, an interaction with the transient section of the guided mode can be realized. The intensity of third-order nonlinear interactions is represented by the nonlinear parameter.

In silicon the third-order nonlinearity can be represented by an electric field **E** that has three frequency components (ω_n):

$$\boldsymbol{E}(\boldsymbol{r},t) = \sum_{n=1}^{3} \boldsymbol{E}_n = \frac{1}{2}\sum_{n=1}^{3}(\boldsymbol{E}_{\omega_n n}(\boldsymbol{r},\omega_n)\boldsymbol{e}^{-i\omega_n t} + c.c.), \tag{2.34}$$

If we substitute Eq. (2.34) into Eq. (2.7) and develop the frequency components of $\chi^{(3)}$, we have new terms for the third-order polarization, $\boldsymbol{P}^{(3)}$, at new frequencies:

$$\boldsymbol{P}^{(3)} = \tfrac{3}{4}\varepsilon_0\chi^{(3)}\left[\left|\boldsymbol{E}_{\omega_1}\right|^2\boldsymbol{E}_1 + \therefore\right]$$

PM

$$+\frac{6}{4}\varepsilon_0\chi^{(3)}\left[\left(\left|\boldsymbol{E}_{\omega_2}\right|^2 + \left|\boldsymbol{E}_{\omega_3}\right|^2\right)\boldsymbol{E}_1 + \therefore\right]$$

PM

$$+\frac{1}{4}\varepsilon_0\chi^{(3)}\left[\left(\boldsymbol{E}^3_{\omega_1}\boldsymbol{e}^{i3\omega_1 t} + c.c.\right) + \therefore\right]$$

$$+\frac{3}{4}\varepsilon_0\chi^{(3)}\left[\frac{1}{2}\left(E_{\omega_1}^2 E_{\omega_2} e^{i(2\omega_1+\omega_2)t}+c.c.\right)+\therefore\right] \quad \text{HG}$$

$$+\frac{3}{4}\varepsilon_0\chi^{(3)}\left[\frac{1}{2}\left(E_{\omega_1}^2 E_{\omega_2}^* e^{i(2\omega_1-\omega_2)t}+c.c.\right)+\therefore\right] \quad \text{WM} \qquad (2.35)$$

$$+\frac{6}{4}\varepsilon_0\chi^{(3)}\left[\frac{1}{2}\left(E_{\omega_1} E_{\omega_2} E_{\omega_3}^* e^{i(\omega_1+\omega_2-\omega_3)t}+c.c.\right)+\therefore\right] \quad \text{WM}$$

$$+\frac{6}{4}\varepsilon_0\chi^{(3)}\left[\frac{1}{2}\left(E_{\omega_1} E_{\omega_2} E_{\omega_3} e^{i(\omega_1+\omega_2+\omega_3)t}+c.c.\right)+\therefore\right] \quad \text{WM}$$

where c.c. means the complex conjugate and the symbol $\therefore$ denotes the possible permutations of frequencies. PM, HG and WG are phase modulation, harmonic generation and wave mixing, respectively. The nonlinear optical excitations are mentioned in Eq. (2.35) and between all these nonlinear processes only those which satisfies energy and momentum conservation (i.e. phase-matching) have efficient excitation (Boyd, 2008).

2.2 Nonlinear Parameters

In nonlinear optics, third-order materials have a profound impact and we can represent the properties of an optical media with a refractive index that depends on the intensity of the optical wave (I):

$$n = n_0 + n_2 I, \qquad (2.36)$$

where n_0 is the refractive index of the material and n_2 represents the second-order nonlinear refractive index that gives the ratio of the variation of the refractive index to the optical intensity (Boyd, 2008). This parameter is related to the third-order nonlinear susceptibility, $\chi^{(3)}$ by (Boyd, 2008):

$$n_2 = \frac{3}{4n_0^2\varepsilon_0 c}\chi^{(3)}, \qquad (2.37)$$

which can be written in Gaussian units as

$$n_2\left(\frac{\mathrm{cm}^2}{\mathrm{W}}\right)=\frac{12\pi^2}{n_0^2 c}10^7\chi^{(3)}(esu)=\frac{0.0395}{n_0^2}\chi^{(3)}(esu) \tag{2.38}$$

In general, in optical waveguides the core and the cover material have a third-order nonlinear susceptibility that can be considered to be nonzero and constant inside the interaction domain and that is zero outside of the nonlinear interaction domain. The interaction domain is defined as the region where the nonlinear materials and the optical field overlap.

Nonlinear effects are related to the intensity of the electromagnetic field in the medium. Moreover, the optical power can be obtained by integrating the intensity distribution over the optical waveguide cross section. If we consider a uniform distribution of intensity, I, over an effective area, A_{eff} in a waveguide with a nonlinear interaction region, D_{inter}, we can express the intensity distribution from the power measured at the output of the waveguide, P_{out} as:

$$I=\frac{P_{out}}{A_{eff},} \tag{2.39}$$

However, the field of an optical waveguide that has been covered by a nonlinear material is unevenly distributed over the waveguide and within the core (Agrawal, 2013b ; Koos, 2007).

Thus, the two important quantities that can be used to study the nonlinear characteristics of a structure are the nonlinear Kerr parameter, $n_2(\mathrm{m}^2/W)$, and the nonlinear waveguide parameter, $\gamma(\mathrm{W}^{-1}/m)$, which are defined as:

$$n_2=\frac{3Z_0}{4n_0^2}\chi^{(3)}, \tag{2.40}$$

$$\gamma=\frac{3\omega\varepsilon_0 Z_0^2}{4A_{eff}n_0^2}\chi^{(3)}=\frac{2\pi}{\lambda}\frac{n_2}{A_{eff}}, \tag{2.41}$$

where Z_0 is the impedance of free space and can be calculated with:

$$Z_0 = \frac{\boldsymbol{E}}{\boldsymbol{H}} = \mu_0 c = \sqrt{\frac{\mu_0}{\varepsilon_0}} = \frac{1}{\varepsilon_0 c}, \tag{2.42}$$

and the effective area, A_{eff} is expressed by:

$$A_{eff} = \frac{Z_0^2 \left| \iint \mathrm{Re}\{\boldsymbol{E}(x,y) \times \boldsymbol{H}^*(x,y).e_z dx\, dy\} \right|^2}{\iint |\boldsymbol{E}(x,y)|^4\, dx\, dy}. \tag{2.43}$$

The nonlinear waveguide parameter, γ, is maximised for strongly confined modes (i.e. smallest nonlinear effective area, A_{eff}, and a large the nonlinear Kerr parameter (Foster, Moll et. Gaeta, 2004 ; Koos *et. al.*, 2007).

2.3 Couple-Mode Theory of Four-Wave Mixing

2.3.1 Origin of Four Wave Mixing

Four-wave Mixing (FWM) is an optical process that originates from the third-order nonlinear susceptibility $\chi^{(3)}$. The FWM process is the nonlinear response of electrons from bound state to an electromagnetic field (Boyd, 2008) and its instantaneous nature makes its adequate for ultra-fast all-optical signal processing.

This parametric process involves four optical waves, three optical signals at different frequencies (ω_1, ω_2, ω_3) and a fourth at a new frequency (ω_4). It obeys the law of conservation of energy and momentum, and it only becomes critical if the phase mismatch between the different signals is very small. When it occurs, energy passes from the pump and signals to the new frequency (idler), and thus, FWM can be used to perform wavelength conversion. The law of conservation of energy is expressed as (Agrawal, 2013a)

$$\omega_4 = \omega_1 \pm \omega_2 \pm \omega_3, \tag{2.44}$$

The phase-matching condition for FWM is $\Delta k = 0$ and can be written as

$$\Delta k = \beta_3 + \beta_4 - \beta_1 - \beta_2, \tag{2.45}$$

$$\Delta k = \left(n_{eff,3}\omega_3 + n_{eff,4}\omega_4 - n_{eff,1}\omega_1 - n_{eff,2}\omega_2\right), \tag{2.46}$$

where $n_{eff,m}$ is the effective index at the frequency ω_i.

To initiate FWM, two pump beams should be launched at two frequencies ω_1 and ω_2. In the the non-degenerate case, these two frequencies are not equal, $\omega_1 \neq \omega_2$, but in the degenerate FWM case (DFWM) that occurs when a single pump beam is present, the frequencies are equal, $\omega_1 = \omega_2$ and one must launch a strong pump beam and a small signal into the waveguide to avoid the depletion of the pump. The waveguide medium interacts with the two beams and as a result it amplifies the signal and creates an idler beam.

Degenerate FWM creates an idler wave at a frequency $\omega_i = 2\omega_p - \omega_s$, in which ω_p, ω_s and ω_i are the carrier frequencies of the pump, signal and idler wave, respectively.

The corresponding mode fields for three frequencies, which are usually very similar, can be expressed as:

$$\boldsymbol{E}(x,y) = \boldsymbol{E}\left(x,y,\omega_p\right) \approx \boldsymbol{E}(x,y,\omega_s) \approx \boldsymbol{E}(x,y,\omega_c), \tag{2.47}$$

$$\boldsymbol{H}(x,y) = \boldsymbol{H}\left(x,y,\omega_p\right) \approx \boldsymbol{H}(x,y,\omega_s) \approx \boldsymbol{H}(x,y,\omega_c), \tag{2.48}$$

2.3.2 Coupled-Mode Theory

As mentioned before, the FWM process originates from the nonlinear polarization caused in the material, and since in this case we have multiple fields interacting, the polarization of each individual field can be written in the form:

$$\boldsymbol{P}_n^{(nl)} = \boldsymbol{P}_n(z)e^{i(\beta_n z - \omega_n t)} \tag{2.49}$$

where $\beta_n$is the propagation constant in the z-direction. From here, the coupled amplitude equations can be solved in the general form (Boyd, 2008):

$$\frac{d\boldsymbol{E}_n}{dz} = \frac{j2\omega_n}{nc}\boldsymbol{P}_n^{(nl)} \tag{2.50}$$

where $\boldsymbol{E}_n$ is the field amplitude at frequency ω_n and it is related to the intensity by $I_n = nc\varepsilon_0|\boldsymbol{E}_n|^2/2$.

In the case of DFWM, the coupled differential equations for a strong pump and low power signal can be written as (Agrawal, 2013b; Hansryd *et. al.*, 2002 ; Lau *et. al.*, 2011 ; Sharping *et. al.*, 2001):

$$\frac{d\boldsymbol{E}_p}{dz} = -\frac{1}{2}[\alpha_{lin}^p + \beta_{TPA}I_p]\boldsymbol{E}_p + i\gamma|\boldsymbol{E}_p|^2\boldsymbol{E}_p, \tag{2.51}$$

$$\frac{d\boldsymbol{E}_s}{dz} = -\frac{1}{2}[\alpha_{lin}^s + 2\beta_{TPA}I_p]\boldsymbol{E}_s + 2i\gamma|\boldsymbol{E}_p|^2\boldsymbol{E}_s + \gamma\boldsymbol{E}_p{}^2\boldsymbol{E}_I^*\exp(i\Delta kz), \tag{2.52}$$

$$\frac{d\boldsymbol{E}_I}{dz} = -\frac{1}{2}[\alpha_{lin}^I + 2\beta_{TPA}I_p]\boldsymbol{E}_s + 2i\gamma|\boldsymbol{E}_p|^2\boldsymbol{E}_s + \gamma\boldsymbol{E}_p{}^2\boldsymbol{E}_I^*\exp(i\Delta kz), \tag{2.53}$$

where β_{TPA} is the TPA at the pump wavelength, α_{lin}^p, α_{lin}^s and α_{lin}^I are the linear propagation loss coefficients of the pump, signal and idler, respectively; $\Delta k = 2\gamma|\boldsymbol{E}_p|^2 - (2k_p - k_s - k_I)$ is the phase mismatch which should be very small for DFWM; k_p, k_s and k_I are the wavenumbers of the pump, signal and idler, respectively; $\gamma = 2\pi n_2/\lambda_p A_{eff}$ is the effective nonlinearity; n_2 is the nonlinear index coefficient; λ_p is the pump wavelength; and A_{eff} is the effective area of the propagating mode.

2.3.2.1 Wavelength Conversion

The conversion efficiency, η, is defined as $\eta = \frac{P_{idler}^{out}}{P_{signal}^{in}}$ and can be evaluated by comparing the power of the signal at the input, P_{signal}^{in}, to the power of the idler at the output of the waveguide. By solving the coupled amplitude equations presented in

section 2.3.2, and assuming efficient phase-matching, the conversion efficiency for DFWM can be written as (Agrawal, 2013b):

$$\eta_{DFWM} = (\mathrm{Re}\{\gamma\} P_{pump} L)^2 \tag{2.54}$$

where P_{pump} is the pump power; L is the interaction length; and γ is the nonlinear parameter (Agrawal, 2013b ; Hansryd *et. al.*, 2002 ; Stolen and Bjorkholm, 1982). Recently, FWM based wavelength conversion experiments were done with SOI waveguides (Foster *et. al.*, 2006 ; Kuo *et. al.*, 2006) but the low conversion efficiency ~ -13 dB is a common problem in all cases.

2.3.2.2 Chromatic Dispersion

Dispersion occurs when the phase velocity of a wave depends on its frequency and, more specifically, chromatic dispersion is the sum of material dispersion and waveguide dispersion. In other words, chromatic dispersion is the interaction of an electromagnetic wave with the bound electrons of a dielectric that depends on the frequency.

When a wave goes through a dielectric medium with a refractive index of n, the light slows to a speed of c/n where c is the velocity of light in vacuum. The phase velocity of a wave, $v_p = \omega/k$, is the velocity with which the phase of a wave propagates in a dielectric medium. However, when light is confined and propagates in a waveguide, the general definition can be rewritten as:

$$v_p = \frac{\omega}{\beta} = \frac{c}{n_{eff}} \tag{2.55}$$

where n_{eff} is the effective index of the guided mode, defined as $n_{eff} = \frac{\beta}{k_0}$. The group velocity can be defined as the velocity at which energy and information propagate along the wave and can be expressed as:

$$v_g = \frac{d\beta}{d\omega}, \tag{2.56}$$

$$\beta_1 = \frac{1}{v_g} = \frac{1}{c}\left(n_{eff}(\omega) + \omega\frac{dn_{eff}}{d\omega}\right) = \frac{n_g}{c} \tag{2.57}$$

where n_g is the group index Eq. (2.57) can be expressed in terms of λ as:

$$n_g(\lambda) = n_{eff}(\lambda) - \lambda\frac{dn_{eff}}{d\lambda}, \tag{2.58}$$

When an optical pulse travels through a waveguide, the group velocity dispersion (GVD) causes pulse broadening and the parameter β_2, which characterises the GVD, can be defined as:

$$\beta_2 = \frac{d^2\beta}{d\omega^2} = \frac{1}{c}(2\frac{dn_{eff}}{d\omega} + \omega\frac{d^2n_{eff}}{d\omega^2}) \tag{2.59}$$

The dispersion parameter, D, with respect to wavelength is represented as

$$D = \frac{d\beta_1}{d\lambda} = -\frac{2\pi c}{\lambda^2}\beta_2 = -\frac{\lambda}{c}\frac{d^2n_{eff}}{d\lambda^2} \tag{2.60}$$

These parameters are critical in nonlinear processes because they define the phase-matching condition in optical waveguides at non-degenerate frequencies.

2.4 Nonlinear Optical Slot Waveguides

A recent breakthrough in integrated optics is the demonstration of the slot waveguide structure, which has two strip waveguides with a high refractive index core material brought close together to form a narrow slot of low index material. Maxwell's equations for high-index-contrast interfaces express that the electric field (**E**) component of the quasi-TE mode must experience a large discontinuity where the amplitude is much higher in the low-index side. The 'slot waveguide' structure confines the light in the region with the lower refractive index (Almeida *et. al.*, 2004). This is the opposite of what happens in standard waveguides where the light is confined in the high index core.

To put it differently, because of the high-index contrast at the two interfaces of the slot and the large electric field discontinuity associated with these interfaces, a

mode with a strong field intensity is created inside the slot. In the center of the slot there is a strong light confinement since the transient end of the strip waveguide modes overlap. Figure 2.4 shows the relative magnitude of the electric field along the *x*-direction across a slot waveguide. The waveguide is made of silicon and the slot and the cladding is air and the light propagates in the *z*-direction. Thus, the slot waveguide enhances the field intensity, which is stronger in the slot than in the core of a similar strip waveguide (Lipson, 2005).

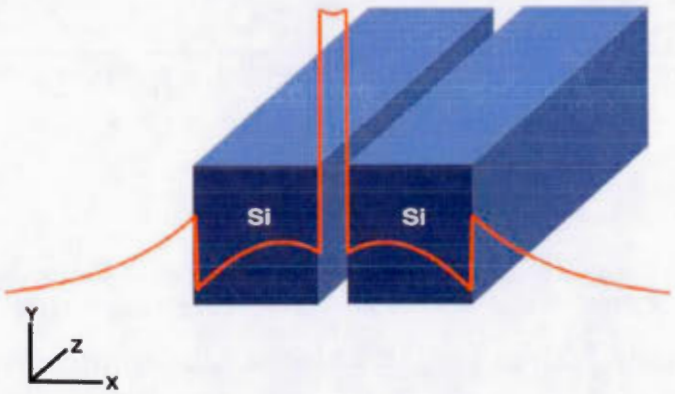

Figure II.4: Schematic of a slot waveguide. The TE-mode (shown in orange) is confined in the low-index slot region [From (Anderson, Schmidt and Lipson, 2006)]

The advantage of slot waveguides is their capacity to confine and guide light in a low-index material, which can be chosen to enable various applications, such as light modulation and detection (Baehr-Jones *et. al.*, 2005), light emission (Barrios et. Lipson, 2005), optical trapping (Yang *et. al.*, 2009) and gas detection (Robinson, Chen et. Lipson, 2008).

There are three waveguide structures that are common to implement nonlinear devices. The first structure is a strip waveguide where the cladding is a nonlinear material; the second is a strip waveguide where the core is the nonlinear material; and the last structure is a slot waveguide where the cladding is a nonlinear material (see Fig. 2.5).

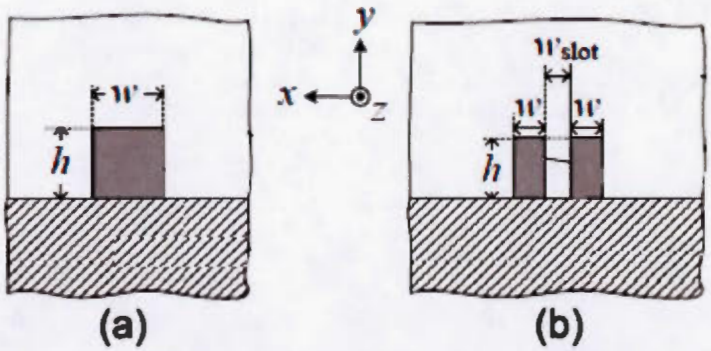

Figure II.5: Cross-section of waveguides a) Strip waveguide (core and cover nonlinearity) b) slot waveguide (cover nonlinearity) [From (Leuthold *et. al.*, 2009)]

Therefore, nonlinear interactions can take place either where the evanescent part of the guided light overlaps with a nonlinear cladding material or inside the waveguide core.

Slot waveguides have an advantage over other waveguide structures due to the fact that they intensify the fundamental quasi-TE mode inside the slot. Thus, when a nonlinear material is present in the slot the nonlinear effects become significant because of the high electric field density in that region. Furthermore, the nonlinearities of the silicon core are no longer dominant since most of the electric field is confined in the slot.

The nonlinear parameters extracted from experimental measurements performed using TE polarized light at different wavelengths for various organic and inorganic cladding materials are summarized in Table 2.1 and 2.2. In this table the nonlinear parameter γ (Koos *et. al.*, 2007) is defined as in Eq. 2.41 in which the real part of γ depends on the waveguide geometry as well as the nonlinear coefficient, n_2, of the interaction material. The linear refractive index, n_0, nonlinear refractive index, n_2, and nonlinear parameter, γ, are taken from the references cited in the tables.

Table II-1: Cladding nonlinearity for inorganic materials (adapted from (Koos *et. al.*, 2007))

Inorganic Materials	$Re\{\gamma\}$ $(Wm)^{-1}$ TE_{slot}	**λ (nm)**	**n_0**	**n_2 (m^2/W)**	**Reference**
Silicon (Channel waveguide)	100	1550	3.48	6×10^{-18}	(Vallaitis, 2014)
Pure silica glass	1.0	1550	1.45	2.48×10^{-20}	(Agrawal, 2013b)
Lead Silicate glass					
Schott SF59	17	1060	1.91	6.8×10^{-19}	(Friberg et. Smith, 1987)
Schott SF57	100	1550	1.8	1.7×10^{-17}	(Vallaitis *et. al.*, 2009)
Chalcogenide glass					
$As_{24}S_{38}Se_{38}$	120	1600	2.45	1.0×10^{-17}	(Cardinal *et. al.*, 1999)
$As_{39}Se_{61}$	105	1500	2.81	1.6×10^{-17}	(Harbold *et. al.*, 2002)
$As_{40}Se_{60}$	151	1500	2.81	2.3×10^{-17}	

Table II-2: Cladding nonlinearity for organic materials (adapted from (Koos *et. al.*, 2007))

Organic Materials	$Re\{\gamma\}$ $(Wm)^{-1}$ / TE_{slot}	λ (nm)	n_0	n_2 (m^2/W)	Reference
PDA	186	1319	~1.5	4.8×10^{-18}	(Rochford *et. al.*, 1991 ; Townsend *et. al.*, 1988)
PTA	78	1907	1.5	2×10^{-18}	(Gubler et. Bosshard, 2002)
TEE	58	1907	1.5	1.5×10^{-18}	(Gubler, 2000)
PSTF66	109	1550	1.5	2.8×10^{-18}	(Asobe *et. al.*, 1995 ; Kaino, 2000)
DANS	293	1319	1.57	8×10^{-18}	(Kim *et. al.*, 1993)
PTS (PDA)	6950	1600	~1.7	2.2×10^{-16}	(Bhowmik et. Thakur, 2001 ; Lawrence *et. al.*, 1994)

In the first group of cladding materials presented, there are various glasses such as lead silicate glasses and chalcogenide glasses that have high linear and nonlinear refractive indices. Thus, the field enhancement in the slot decreases as a result of their high linear index (see Eq. 2.41). Accordingly, the effective area A_{eff} increases and the nonlinear parameter decreases. In Table 2.2, organic materials with a high

nonlinearity due to chromophore units or to the polymer backbone were used as the cladding material.

The conjugated polymer poly(diactelyne-bis-tolune-sulfonide) (PTS) has by far the largest third-order nonlinearity (Bhowmik et. Thakur, 2001 ; Lawrence *et. al.*, 1994). However, this material is challenging to synthesize as a single-crystal film because the PTS molecules must be aligned to maximize nonlinear effects (Thakur et. Krol, 1990). Hence, PTS is not a suitable polymer to be used as a cladding material because it needs to be prepared as a single crystal monomer, and then polymerized. Therefore, it is preferable to use other materials that can be deposited simply by spin-coating (Luther-Davies et. Samoc, 1997).

2.5 Multidirectional Charge-Transfer Transitions Molecules

In this section, the interaction of a single molecule with an electromagnetic field is reviewed. The first order hyperpolarizability β_{ijk} and the second order hyperpolarizability γ_{ijk} of a molecule defined as x are described in terms of the electronic excited states (energy levels) and this energy can be expressed as $E_x - E_g = E_{xg}$ above the ground state (E_g) (Kuzyk, Singer et. Stegeman, 2013).

In the following sections, the electronic and solid-state structures of organic compounds are described to provide a good understanding of nonlinear optical properties in integrated optics technology (Williams, 1984). Organic molecules and polymeric compounds have generated great interest in this field because of their strongly delocalized π electronic systems, which in some materials shows large nonlinear coefficients (Shettigar *et. al.*, 2007). Hence, the electronic origins of nonlinear optical effects for organic π electrons with conjugated double bond systems are discussed.

2.5.1 Molecular Hyperpolarizability

Molecules with conjugated π electronic systems and charge asymmetry have large values of molecular hyperpolarizability. These large values are obtained when the molecule has substituents that bring low-lying charge-transfer resonance states (Gregory, 2012).

The polarization **P** created in a molecule by a local electric field **E** can be calculated from:

$$\mathbf{P} = \alpha\mathbf{E} + \beta\mathbf{E} + \gamma\mathbf{E} + \cdots \tag{2.61}$$

where α, β and γ are linear polarization, first order hyperpolarizability and second order hyperpolarizability, respectively. We can rewrite the Eq. (2.35) in a macroscopic polarization form as:

$$\mathbf{P} = \chi^{(1)}\mathbf{E} + \chi^{(2)}\mathbf{E} + \chi^{(3)}\mathbf{E} + \cdots \tag{2.62}$$

where $\chi^{(1)}$, $\chi^{(2)}$ and $\chi^{(3)}$ are the first-, second-, and third-order nonlinear optical susceptibilities. The second-order nonlinearity, $\chi^{(2)}$, is zero in centrosymmetric media.

The relation between the microscopic and macroscopic nonlinearities can be derived through local field factors (Kajzar *et. al.*, 1987), as in the following equations:

$$\chi^{(1)}(-\omega\,;\omega) = N\alpha f_\omega f_\omega \tag{2.63}$$

$$\chi^{(2)}(-2\omega\,;\omega,\omega) = N\beta f_{2\omega} f_\omega f_\omega \tag{2.64}$$

$$\chi^{(3)}(-3\omega\,;\omega,\omega,\omega) = N\gamma f_{3\omega} f_\omega f_\omega f_\omega \tag{2.65}$$

where N is the number of molecules per volume unit and f_ω is the Lorentz local field factor at frequency ω, which determines the value of the electric field at the site of the molecule (Flytzanis, 1975). For isotropic media the f_ω is given by

$$f = (n^2 + 2)/3 \tag{2.66}$$

where n is the refractive index of the medium.

The relation between $\chi^{(3)}$ and γ for nonlinear optic processes can be written as (Zhao, Singh et. Prasad, 1988):

$$\gamma = \frac{\chi^{(3)}}{Nf^4} \tag{2.67}$$

Thus, one can predict the third-order nonlinear optical susceptibility from calculated second hyperpolarizabilty values.

2.5.2 Third-Order Nonlinear Chromophores

Nonlinear optical chromophores are conjugated π-systems with donor and acceptor components as terminal substituents that results in high values of hyperpolarizability. The efficiency of these molecules such as p-nitroaniline is limited by the unidirectional dipole moment (see Fig. 2.6). This issue can be avoided by using non-dipolar two-dimensional (octupolar) nonlinear optical chromophores.

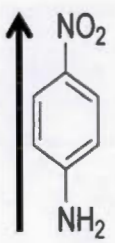

Figure II.6: Molecular structure of p-nitroaniline with unidirectional charge transfer (("4-Nitroaniline ", n.d.))

The nonlinearity in systems with high values of second-order hyperpolarizability γ originates from the conjugated and highly polarized π-electron backbone. It has been found that in donor-acceptor-substituted tetraethynylethenes there are two-dimensional conjugation and donor-acceptor conjugation paths that provide information into routes leading to third-order nonlinear optics (Bosshard *et. al.*, 1996 ; Greve *et. al.*, 1997).

CHAPTER III

MATERIALS AND FABRICATION

Highly nonlinear integrated waveguides can be realized by employing an appropriate interaction material. Studies have shown that molecules with multidirectional charge transfer transitions show larger hyperpolarizabilities than molecules with unidirectional charge transfer transitions (Zyss *et. al.*, 1991 ; Zyss *et. al.*, 1993). Thus, chromophores with three-fold symmetry such as crystal violet that have multiple donor-acceptor substituents can achieve high hyperpolarizabilities.

In this chapter, we will discuss the nonlinear material used for filling the slot waveguides, the device design, the fabrication process and finally the spin coating process used for the deposition of crystal violet on the slot waveguides.

3.1 Materials

3.1.1 PMMA

Poly(methyl methacrylate) (PMMA) is an important material that is often used to form membranes in optical applications and in electron beam lithography (Park and. Lakes, 2007). It is a single-copolymer from the family of polyacrylic and methacrylic esters and due to its properties, such as optical transparency, high strength and good dimensional stability; it is a suitable material as a negative resist (Huang and Brittain, 2001; Semaltianos, 2007; Wang *et. al.*, 2001). PMMA, which has a refractive index of 1.49 at the telecommunication wavelength λ=1550 nm, can also be used as a cladding layer on silicon waveguides, as a protective layer for wafer thinning, as a sacrificial layer or as a bonding adhesive.

3.1.2 Crystal Violet

In order to obtain a large second-order hyperpolarizability γ, molecules with multidirectional intramolecular charge-transfer (CT) transitions can be used instead of unidirectional molecules since in multidirectional molecules their charges move from the periphery to the center of the molecules under the action of a polarisation field. However, in unidirectional molecules, charges are displaced along the length of the molecule, which results in a simple dipole. Therefore, large changes in electric moments will appear in molecules with multidirectional intramolecular charge-transfer (CT) transitions as a consequence of molecular symmetry, which enables periphery-to-center charge-transfer transitions (Greve *et. al.*, 1997).

Periphery-to-center charge-transfer transitions can be observed in tris(4-N N-dimethylaminophenyl)methyl, which is better known as crystal violet. Its chemical structure is presented in Fig. 3.1 and consists of a central carbon atom bonded to three benzene rings that are in turn each linked to a methyl group. The dialkylamino group in the periphery of the molecule are the electron donors and the central carbocation acts as the acceptor.

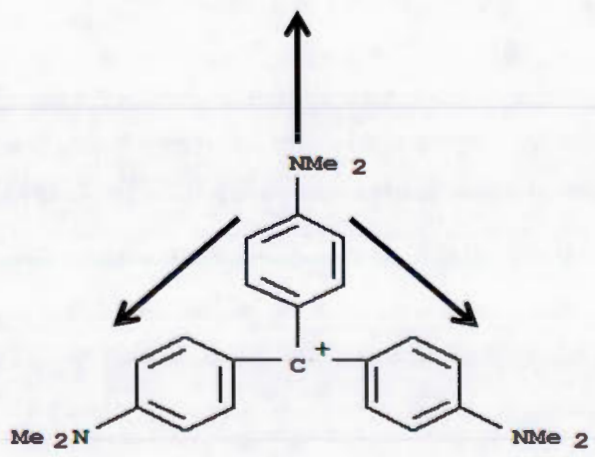

Figure III.1: Molecular structure of crystal violet [from (Greve *et. al.*, 1997)]

The periphery-to-center charge-transfer (PC-CT) is consistent with the HOMOs and LUMOs states of crystal violet, which are illustrated in Fig. 3.2 (Greve et al., 1997).

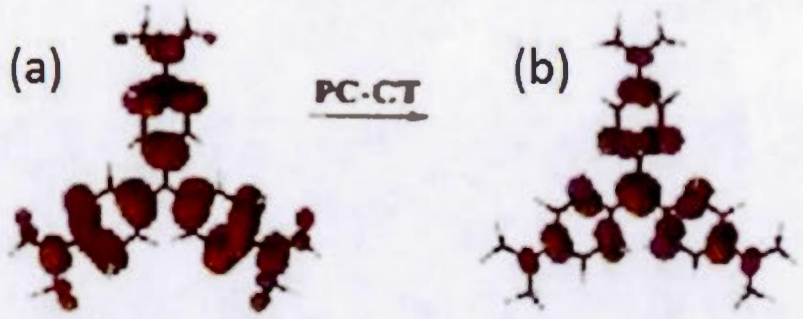

Figure III.2: Calculated a)HOMO and b) LUMO for crystal violet[from (Greve *et. al.*, 1997)]

The second-order hyperpolarizability of crystal violet molecules was evaluated based on third harmonic generation measurements made with thin films. Previous studies reported high γ-values for this chromophores around $\gamma = 2.0 \times 10^{-33}$ esu at a wavelength of λ=1064 nm (Greve *et. al.*, 1997).

3.2 Silicon Slot Waveguides

3.2.1 Waveguide Design

The slot waveguides that were used for this thesis were designed by Dr. Mohamed Rahim. In the design of slot waveguides, the critical factors that must be considered are the slot orientation (vertical or horizontal), the waveguide geometry, and the choice of materials. The silicon-on-insulator structure typically used in silicon photonics (Bogaerts *et. al.*, 2007), which consists of a thick buried oxide layer (~2 to 4 μm) and a thin crystalline silicon layer (220 nm), provides the high refractive index

contrast that is necessary to implement slot waveguides. Moreover, as described below, commercial processes that offer multi-project wafer runs are available for this technology. The process provided by IMEC was used to implement the sample presented in Fig. 3.3.

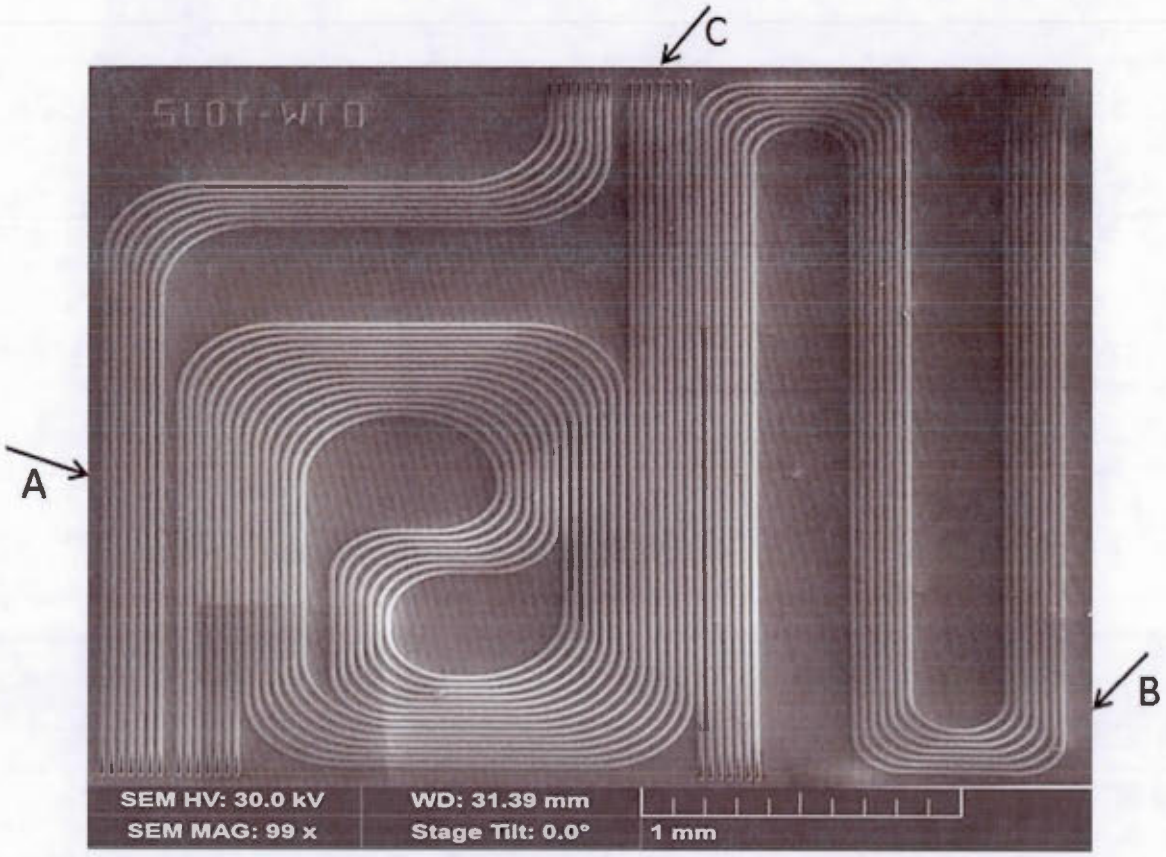

Figure III.3: Top-view SEM picture of design. The letters refer to Table 3.1.

The waveguides in the device shown in Fig. 3.3 can be divided into three blocks of seven waveguides, which have different geometries as indicated in Table 3.1. Each block has waveguides of different lengths and each also has curves with different radii. The device parameters for three blocks are presented in Table 3.1.

Table III-1: Waveguides' dimensions

	Slot waveguide's width (μm)		Waveguides dimensions (μm)		
Waveguides	**A-100**	W_s=0.10	**Block A**	**Length**	**Curves' radii**
	A-120(1)	W_s=0.12		L_1=3726	R_1=300.32
	A-120(2)	W_s=0.12	**Block B**	L_2=9369.5	R_2=150.32
	A-130	W_s=0.13			
	A-140	W_s=0.14			
	Y-100	W_s=0.10	**Block C**	L_3=12396	R_3=190.32
	Y-120	W_s=0.12			R_1=290.32

In this study, the thickness of the silicon layer used to build the slot waveguides is h=220 nm (see Fig. 3.4). The rail width is constant for all waveguides at w_r=240 nm but the slot width varies between w_s =100-140 nm (see Fig. 3.4). Thus, each block has waveguides with various slot widths. The slot filling material in this experiment, PMMA containing crystal violet, is assumed to have a refractive index of 1.51 at a wavelength of 1550 nm.

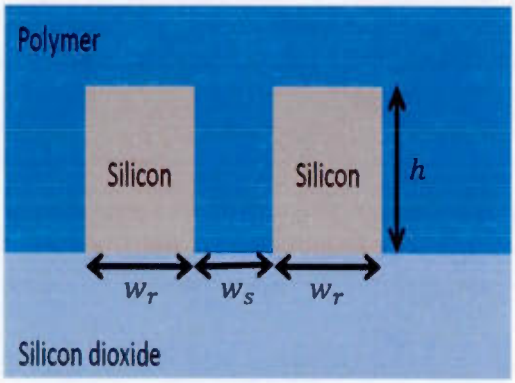

Figure III.4: Slot waveguide structure

In addition to different slot widths, two types of couplers were used to perform the transition between the strip waveguides connected to the grating couplers (described below) and the slot waveguides. Optical couplers are passive devices that couple light between waveguides and they have been used in many applications including the interface between devices (Liu, 2005). In this experiment they are used to transform the fundamental mode of the input and output channel waveguides to the mode supported by the slot waveguide. The first type of coupler used is a simple Y-branch. There are two waveguides with Y-branch couplers in each of the 3 blocks of this device. They are identified by the letter Y in Table 3.1. Figure 3.5 shows a scanning electron microscopy (SEM) top-view of the Y-branch. The parameters of the Y-branch are as follows: rail width before separation w= 600 nm, waveguides separation in the range of w_s=100 -120 nm and rail width w_r=240 nm.

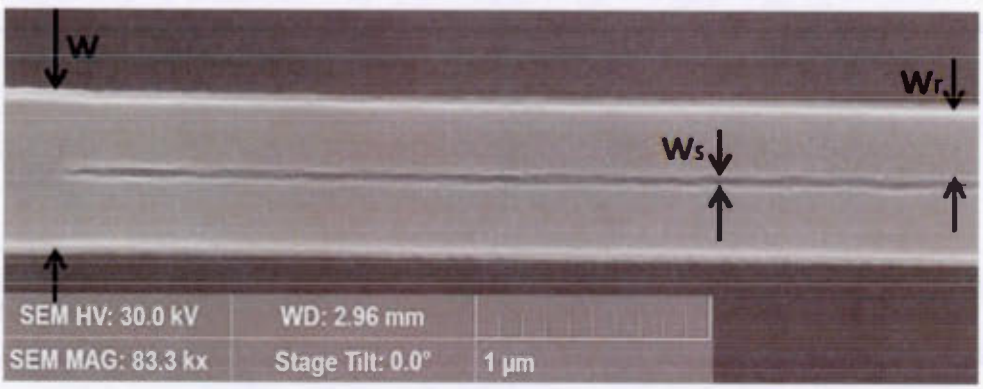

Figure III.5: Top-view SEM picture of the Y-branch

Y-branch couplers are simple to design and have been used in numerous demonstrations. However, their performance is limited by the minimum feature size achievable with a given fabrication process, which leads to an abrupt transition from strip to slot waveguide. To improve the performance of the transition region, couplers with an adiabatic transition from strip to slot waveguide were used in most of the waveguide implemented on the samples used for this work. The design of these adiabatic couplers (shown in Fig. 3.6) is based on the work reported by Säynätjoki *et. al.* (2011). The strip waveguide is progressively narrowed down into one of the rails of the waveguide within the coupler length. The upper slot rail has an initial width w_t=100 nm, which enlarges gradually to the final rail width. The adiabatic couplers have the following design parameters: waveguide length L=4 μm, waveguide width W=450 nm and waveguides separation S=240 nm.

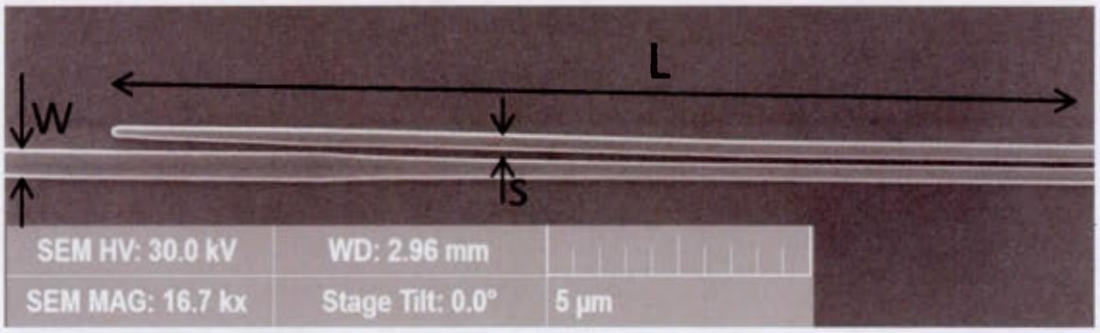

Figure III.6: Top-view SEM picture of the coupler design used in sample

Because of the optical mode mismatch at the interface between an optical fiber and a silicon photonic device, grating couplers are used to couple light from an optical fiber to a waveguides (Suhara and Nishihara, 1986). The diffraction in the grating structure changes the direction of propagation of the light coming from the input fiber to send it along the silicon strip waveguide. The inverse happens at the output side. Figure 3.7 and 3.8 show the grating couplers that are located at the two ends of each waveguide on the sample. They are 10 μm × 10 μm in size and convert the fiber mode into a 10 μm wide mode that than travel along an adiabatic taper until it reaches the width of the strip waveguide (500 nm). The grating dimensions must be

large enough to collect the entire incident laser beam from the optical fiber. The grating period is designed for light incident at 10°, which ensures that the light is propagating towards the desired direction in the waveguide (Pello, 2014).

Figure III.7: Top-view SEM picture of grating coupler

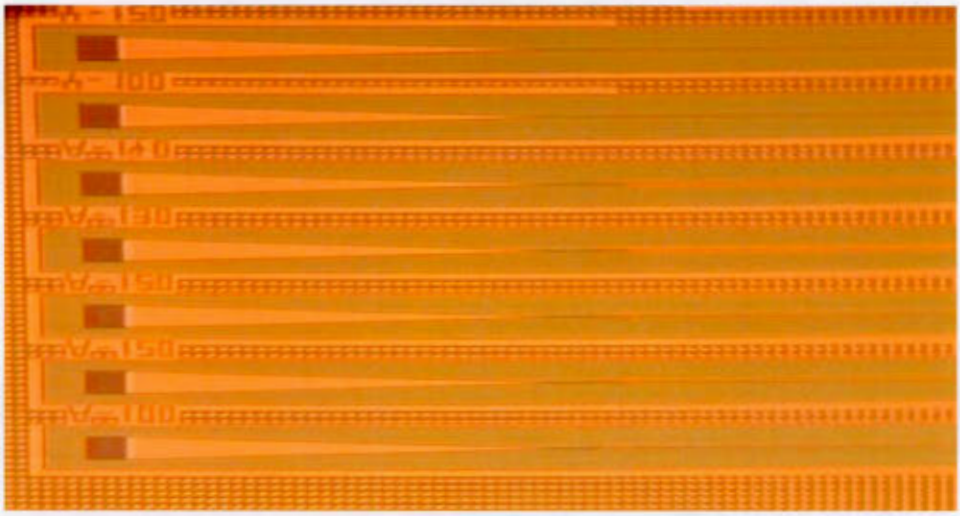

Figure III.8: Image of the grating couplers at the end of one block of waveguides

3.2.2 Device Fabrication

The chip was fabricated at the IMEC foundry through an academic collaboration with CMC Microsystems. In this section, the process and design rules of the silicon photonic chips is described based on the documentation for IMEC silicon photonics technology, which is referred to as SIPP (Dumon, 2012).

The SIPP technology uses SOI wafers with the following specifications:

- 220 nm crystalline (100) Si top layer with a background P-doping of boron,
- 2000 nm buried oxide,
- 725 μm substrate with a background P-doping of boron.

The process flow is divided into different modules, which regroup all the steps required to transfer a pattern onto the wafer (i.e. lithography, etching, cleaning, etc.). These modules create passive device structures into the SOI layer, and in the case of our samples, two of these process modules are needed to produce the waveguides and the grating couplers. The waveguide (WG) module etches 220 nm trenches and holes into the silicon device layer until the buried oxide is reached (see Fig. 3.9). The patterns are defined using 193 nm deep ultraviolet (DUV) lithography. This module can be used to create strip waveguides, photonic crystals, ring resonators, Bragg gratings with side modulations or arrayed waveguide gratings.

The fiber coupler (FC) module etches 70 nm into the silicon device layer and the patterns are also defined using 193 nm DUV lithography. The FC module can be used for many structures, such as rib waveguides, star couplers and Bragg gratings with top modulation (see Fig. 3.9).

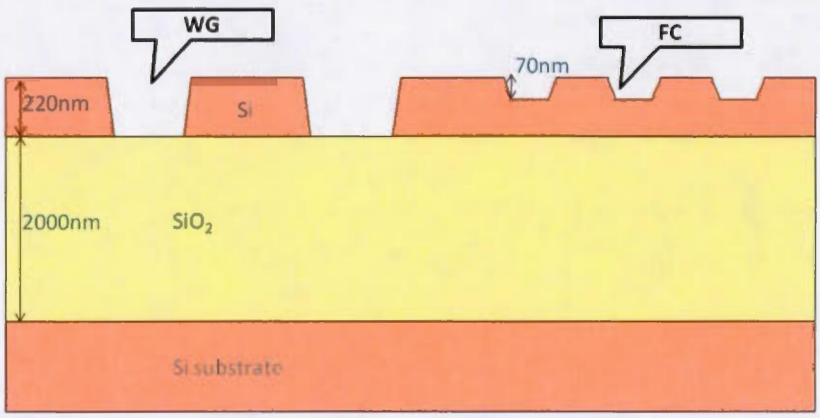

Figure III.9: Cross-section of SiPhotonics Standard Passives (PSV) FC and WG modules (Dumon, 2012)

Lastly, a 5 μm thick protective resist top cladding (RESCLAD) is applied on the wafer, as shown in Fig. 3.10. The wafer can also be cladded with silicon dioxide but in this work we needed to have access to the surface of the waveguide core. The protective resist is removable with acetone and isopropyl alcohol. An overview of the process modules is described in Table 3.2.

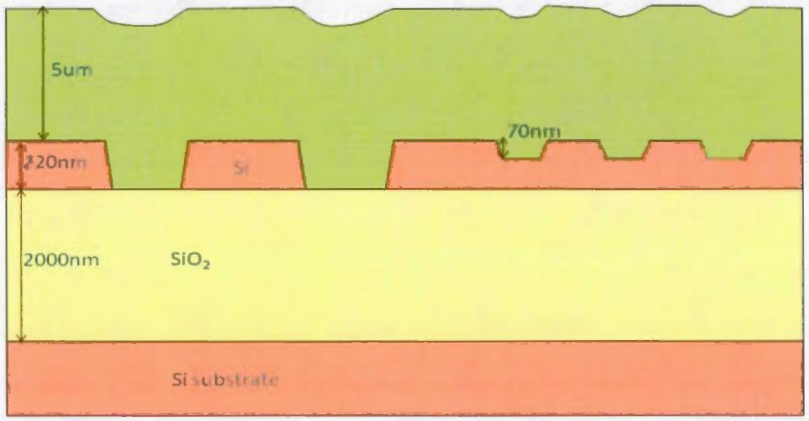

Figure III.10: Cross-section of SiPhotonics PSV with resist cladding (Dumon, 2012)

Table III-2: Overview of process modules

Process Module	Description
FC	70 nm deep trenches/holes/ribs.
WG	220 nm deep trenches/holes/strips.
RESCLAD	5 μm protective resist cover.

The complete SiPhotonics PSV process flow is as follows:

1. Cleaning
2. FC
3. WG
4. RESCLAD
5. Dicing

3.2.3 Deposition of Crystal Violet

Solution Preparation

In general, PMMA is formulated with a molecular weight of 120K, 495K or 950K and the usual method for its deposition is spin coating. In this work, different concentrations of PMMA and crystal violet were studied to optimise the slot waveguide-polymer integration. In recent studies crystal violet 10 wt. % has been used for the study of third-order nonlinearities. Thus, different concentrations of crystal violet from 1 to 10 wt. % have been prepared to deposit on the samples for the further experiments (see Chapter 4).

The crystal violet and PMMA solutions were prepared with two different solvents. The solutions were prepared by following these steps:

- For 5 wt % PMMA: 150 mg of PMMA 120K from Sigma-Aldrich were dissolved in 3 ml of solvent (i.e. chlorobenzene or chloroform),
- For 1 to 10 wt % crystal violet: 30 mg of crystal violet per percent were dissolved in a 5 wt % PMMA solution.

Each solution was stirred for three hours at 40 °C with a magnetic stirrer/hot plate, and then it was placed in an ultrasonic bath for 30 minutes to make sure the solutions were uniform.

The first concentration that was prepared was the 10 wt. % crystal violet solution. It was deposited on a sample but because of the thickness and opaqueness of this high concentration, the waveguides could not be seen with the visible camera, which made it impossible to align the optical fibers with the waveguides. Thus, lower concentrations of crystal violet solutions in chlorobenzene were tested from 1 to 5 wt. % for the study of propagation loss (see Chapter 4) but measurements were obtained only for the 1 wt.% crystal violet due to the viscosity and opaque color of higher concentrations.

Another issue that arose with the crystal violet solutions made with chlorobenzene is that the solubility of crystal violet is limited in this solvent. As

shown in Fig. 3.11, the sample is not uniform and it has crystal violet particles that are not dissolved.

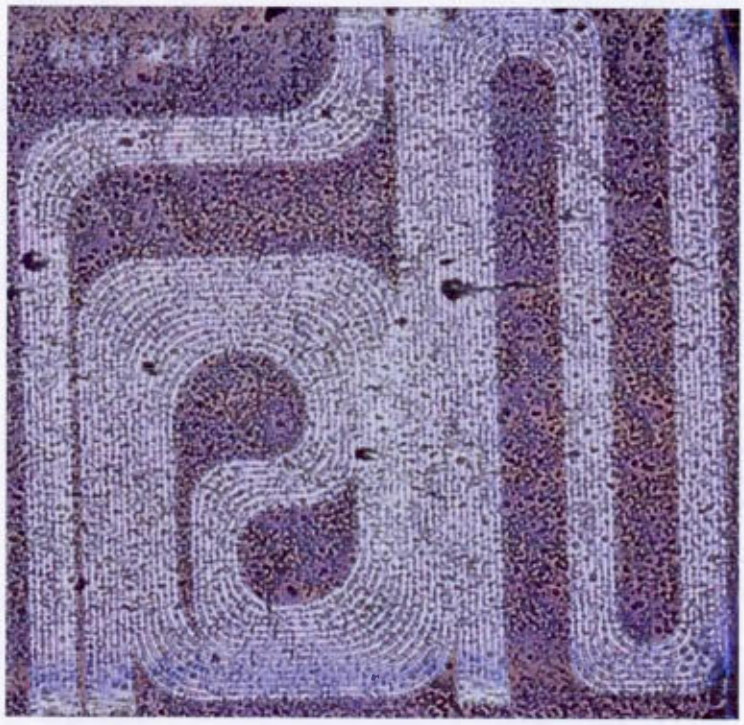

Figure III.11: Sample covered with crystal violet 5 wt % dissolved in chlorobenzene

Therefore, chloroform was chosen to replace the previous solvent in order to better dissolve the PMMA and crystal violet (Al-Kadhemy and Abaas, 2012). In addition, to remove undissolved particles, a 450 nm filter was used to deposit the solution. In comparison with the chlorobenzene solution, the chloroform solution is more uniform and the grains have disappeared, as shown in Fig. 3.12.

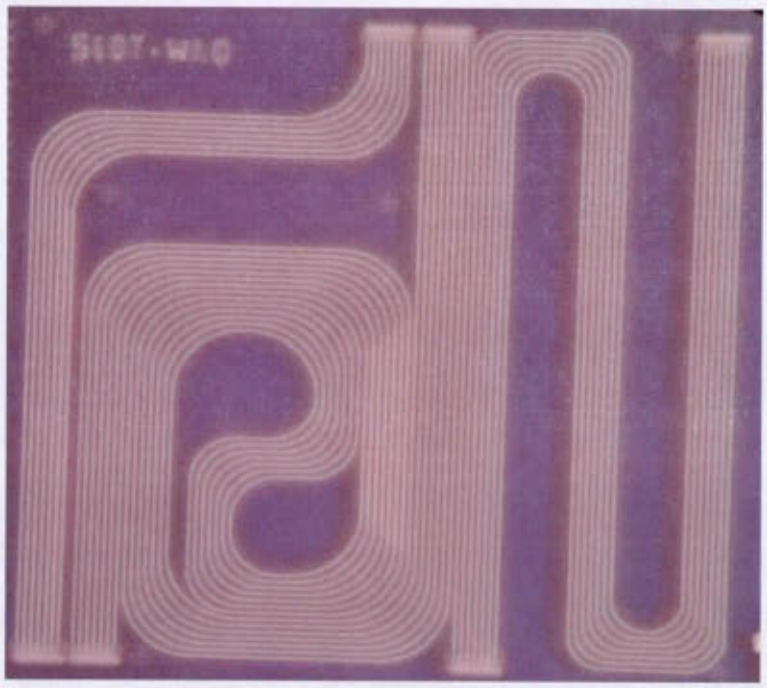

Figure III.12: Sample covered with crystal violet 5 wt. % dissolved in chloroform

Finally, to make sure that the slot waveguides are filled with the cladding material, samples with 5 wt. % PMMA and 1 wt. % crystal violet were cleaved and their cross-section was imaged with SEM. Figure 3.13 and 3.14 show that the slot waveguides are properly filled with the solutions.

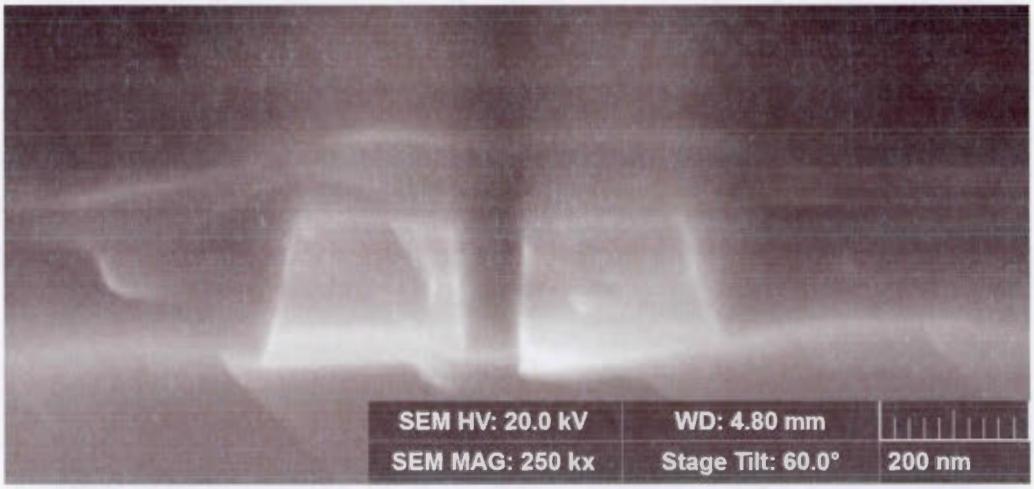

Figure III.13: SEM picture of the cleaved sample deposited with 5 wt. % PMMA

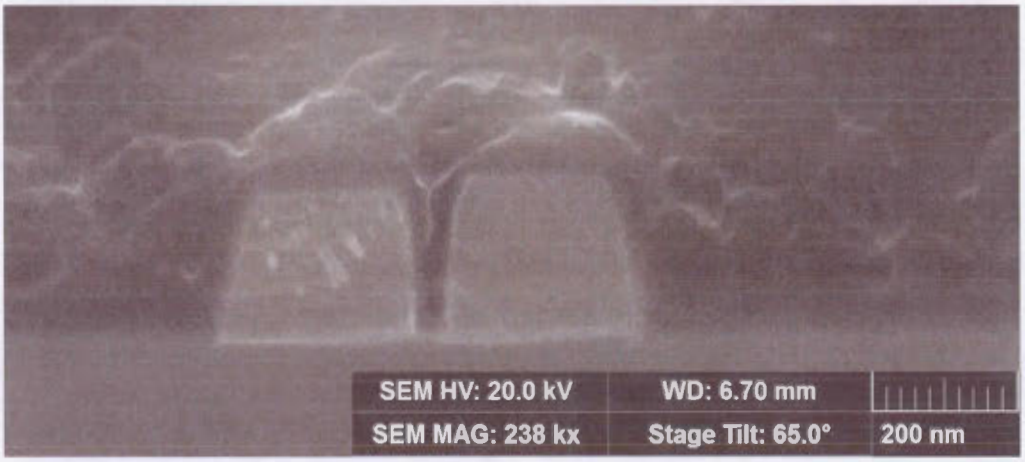

Figure III.14: SEM picture of the cleaved sample deposited with 1 wt. % crystal violet

Cleaning of the Samples

The samples had to be prepared before the polymer deposition. They were cleaned with acetone, isopropyl alcohol and deionized (DI) water in successive steps and then they were dried with nitrogen. This was required in order to remove the photoresist and to clean any possible contamination.

Hence, sample cleaning is one of the most important aspects of the fabrication process to remove the contamination and it was done as follows:

- Dipping in acetone for 5 minutes,
- Dipping in isopropyl alcohol for 5 minutes,
- Dipping in DI water for 5 minutes,
- Blow drying with nitrogen,
- Baking at 150°C for 10 min on a hotplate to dehydrate the sample.

Before proceeding to the deposition, it is important to verify that there are no dust particles on the sample by inspecting it under the microscope.

Spin Coating Deposition

To begin the deposition, a puddle of crystal violet solution (3-5 ml) is placed at the centre of the sample, and then spun to form a uniform layer of crystal violet. The resulting film thickness depends on the solution viscosity, the ramp of speed and most importantly the final spin speed.

The crystal violet solution was spin coated onto the sample in 2 steps with the following parameters:

Step 1:

Spin speed: 1500 rpm

Ramp: 750

Time: 10 sec

Step 2:

Spin speed: 3500 rpm

Ramp: 750

Time: 35 sec

After this, the sample is baked on a hotplate at a temperature of 130°C for 120 seconds. This soft bake is done to harden the solution and to improve uniformity. Again, it is necessary to make sure that there is no dirt or scratch on the sample under the microscope before performing any measurement.

CHAPTER IV

THIRD-ORDER NONLINEAR EFFECT IN SOI WAVEGUIDES

In this chapter, the Eigenmodes of slot waveguides and the transverse electric field distribution of the quasi-TE mode are simulated by using a full-vectorial finite-difference mode solver. In the following section, by using the extended definition of A_{eff}, we calculate the effective mode area for slot waveguides with different slot widths. The waveguide geometries considered here are those of the fabricated samples, which were based on configurations previously reported in the literature for other hybrid demonstration. The waveguides were fabricated before the simulations were completed because of the time frame imposed by the fabrication runs offered through CMC Microsystems. Next, the nonlinear waveguide parameter γ is estimated for waveguides with a crystal violet cladding based on values reported in the literature for crystal violet thin films. The material parameters and nonlinear coefficients of crystal violets are summarized in this chapter. The last part of this chapter deals with FWM-based wavelength conversion, which is simulated with a MATLAB script that solves the nonlinear coupled mode equations presented in chapter 2.

4.1 Numerical Calculations of Slot Waveguide Modes

In order to study the effect of the nonlinear material in the slot region, the modal distribution of the slot waveguides must be analyzed and the effective refractive index n_{eff} of the guiding mode must be calculated. Simulations were performed using the Beam Propagation Method (BPM) provided with the RSoft package, which offer

a full spectrum of photonic devices and optical communication design solutions. As mentioned in chapter 2, this method approximates the wave equation and solves the resulting equations numerically by using finite difference methods.

The slot waveguide structure simulated in RSoft, including its refractive index distribution, is presented in Fig. 4.1.

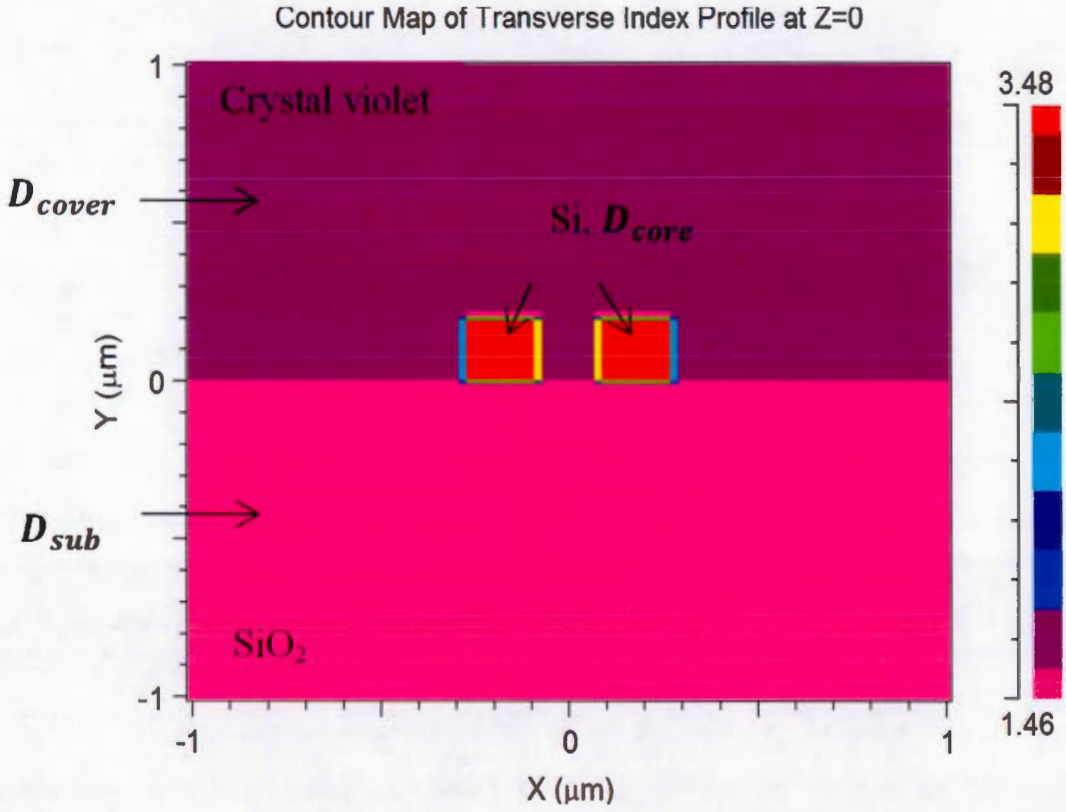

Figure IV.1: Counter map of transverse index profile of a slot waveguide with crystal violet cladding. The colour scale represents the refractive index value

In our case, the main E-field component of the guided mode in the slot waveguide is along the *x*-direction and corresponds to the quasi-TE Eigenmode. By using the RSoft software, the quasi-TE Eigenmode of the slot waveguide structure can be simulated with a full-vectorial finite-difference mode solver and a non-uniform mesh. As mentioned before, the slot waveguide is built on a silicon-on-insulator (SOI) substrate. The slot waveguide core is made of silicon that has a refractive index of

n_{Si}=3.48, and it is supported by a lower cladding in SiO_2 that has a refractive index of n_{SiO_2}=1.46. In the simulations, the wavelength is assumed to be λ=1.55 μm with a slot width, w_s filled with a low-index material, crystal violet (n_{CV}=1.51) and a defined height h. The slot waveguide structure has rails having a width of w_r=240 nm, a slot with a width between w_s= 110 to 140 nm, and a height of h=220 nm. The range of slot width was limited between 110 nm and 140 nm for two reasons: the smallest dimension was dictated by the minimum feature size used to implement the sample presented in chapter 3; the maximum dimension on the other hand was set by the fact that for slot widths of more than w_s >140 nm, the efficiency drops significantly. A grid spacing of 0.1 μm is used by the complex mode solver within the region that includes the waveguide. Figure 4.2 shows a scanning electron microscopy (SEM) top-view picture of a fabricated slot waveguide structure indicating the dimensions corresponding to the rail width (w_r) and the slot width (w_s).

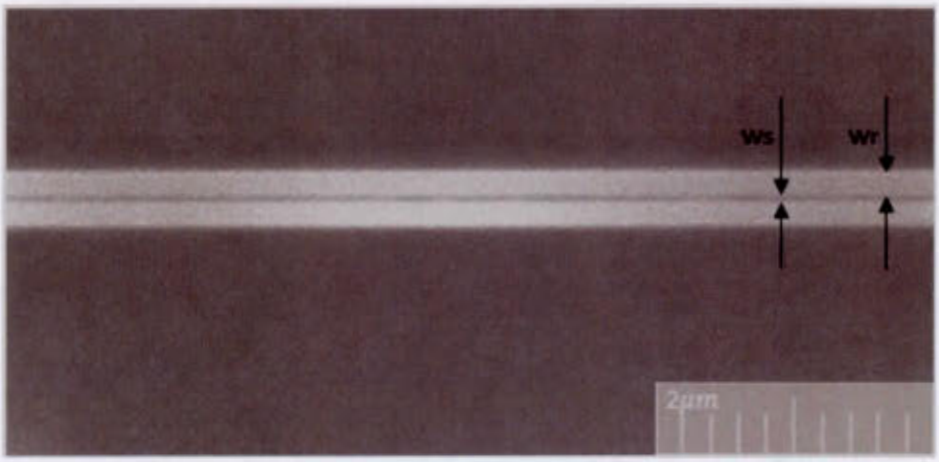

Figure IV.2: Top-view SEM picture of the slot waveguide

The transverse E-field amplitude distribution of the guided quasi-TE mode is shown in Fig. 4.3 for different slot width. The strong E-field in the slot is noticeable by the bright region in center. As explained in chapter 2, this is due to the overlap of the strong discontinuity caused by the high-index contrast interfaces that are very close to each other.

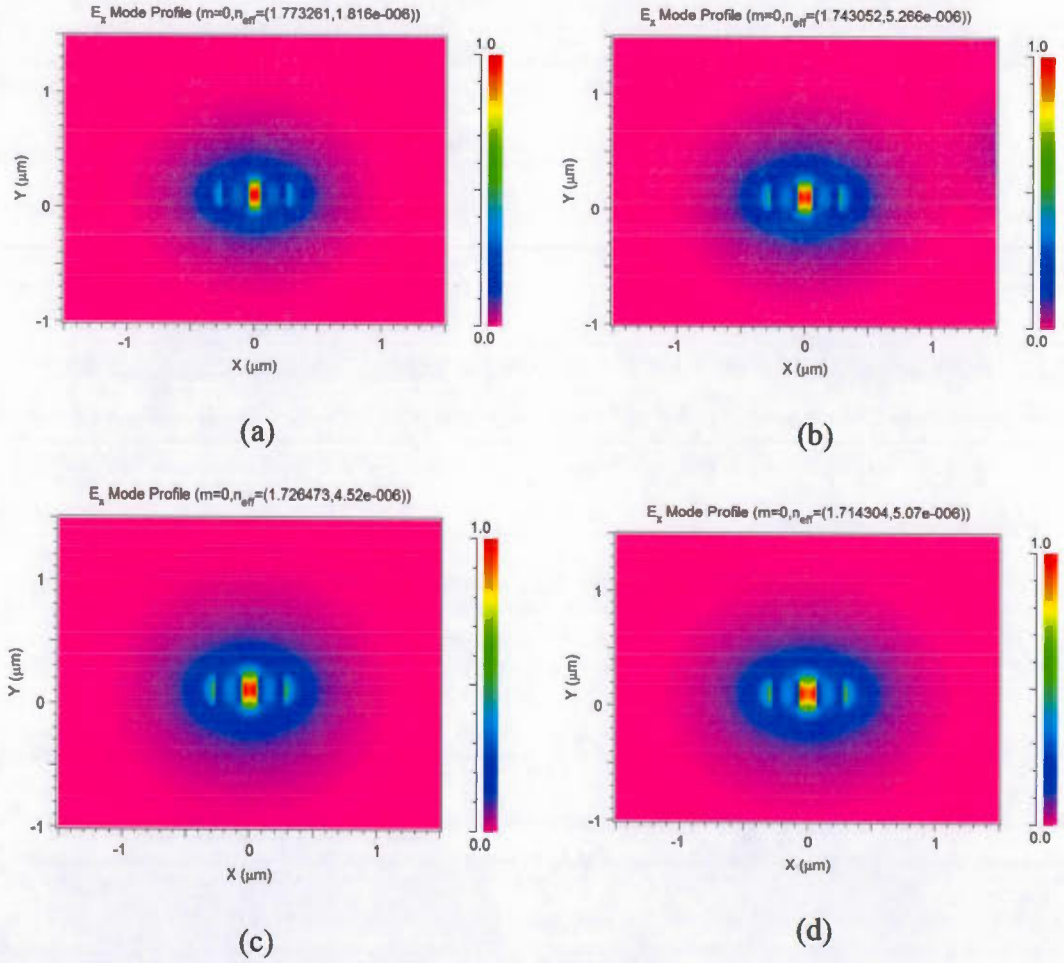

Figure IV.3: Normalized transverse E-field profile of the quasi-TE mode for n_{cover}=1.51 for a) w_s=100 nm b) w_s=120 nm c) w_s=130 nm d) w_s=140 nm. The color scale shows the electric field normalised amplitude.

The effective refractive index of the slot waveguide Eigenmode calculated through simulation is listed in Table 4.1 for different slot width considered in this study.

Table IV-1: Effective refractive index of crystal violet for different slot width

w_s (nm)	n_{eff}
100	1.77
120	1.74
130	1.72
140	1.71

Also, the n_{eff} variation as a function of wavelength for different slot widths is shown in Fig 4.4.

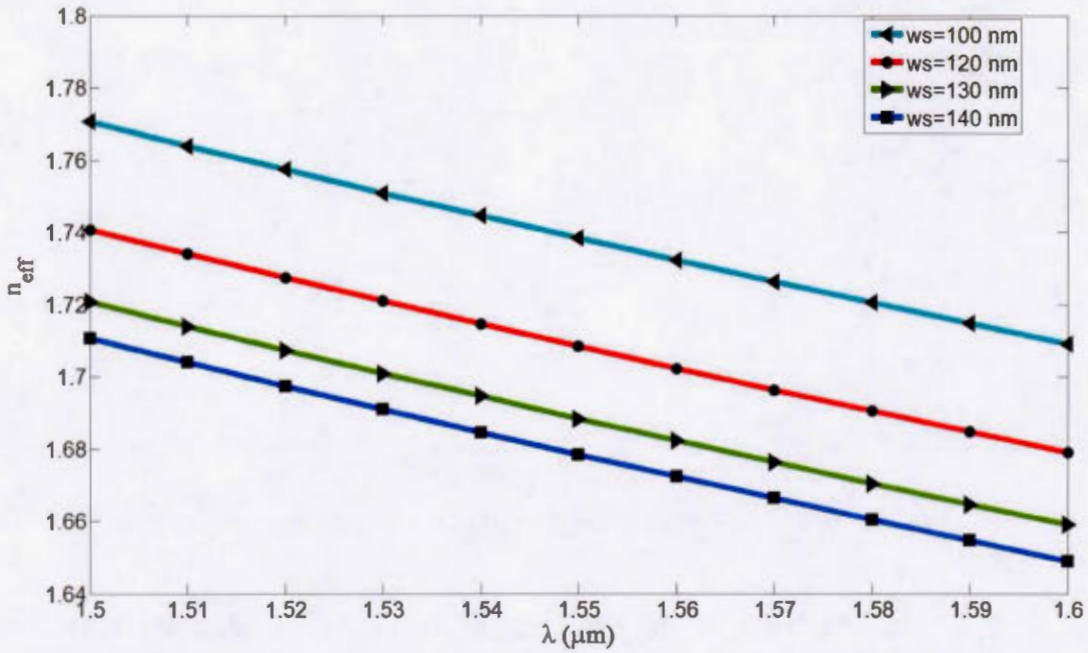

Figure IV.4: Effective refractive index of crystal violet as a function of wavelength for for various slot widths 100 nm<w_s<140 nm

Therefore, since the effective refractive index is significantly lower that the refractive index of silicon, this shows that the optical power for the quasi-TE mode is concentrated in the slot. Furthermore, the effective refractive index is smaller than that of comparable channel waveguides (Xu et al., 2004).

The horizontal cut of the major component of the E-field is shown along the x-direction at y=0 in Fig. 4.5. It can be seen that the optical intensity in the slot region is much higher than that in the high-index regions, which demonstrate the E-field enhancement provided by slot waveguides.

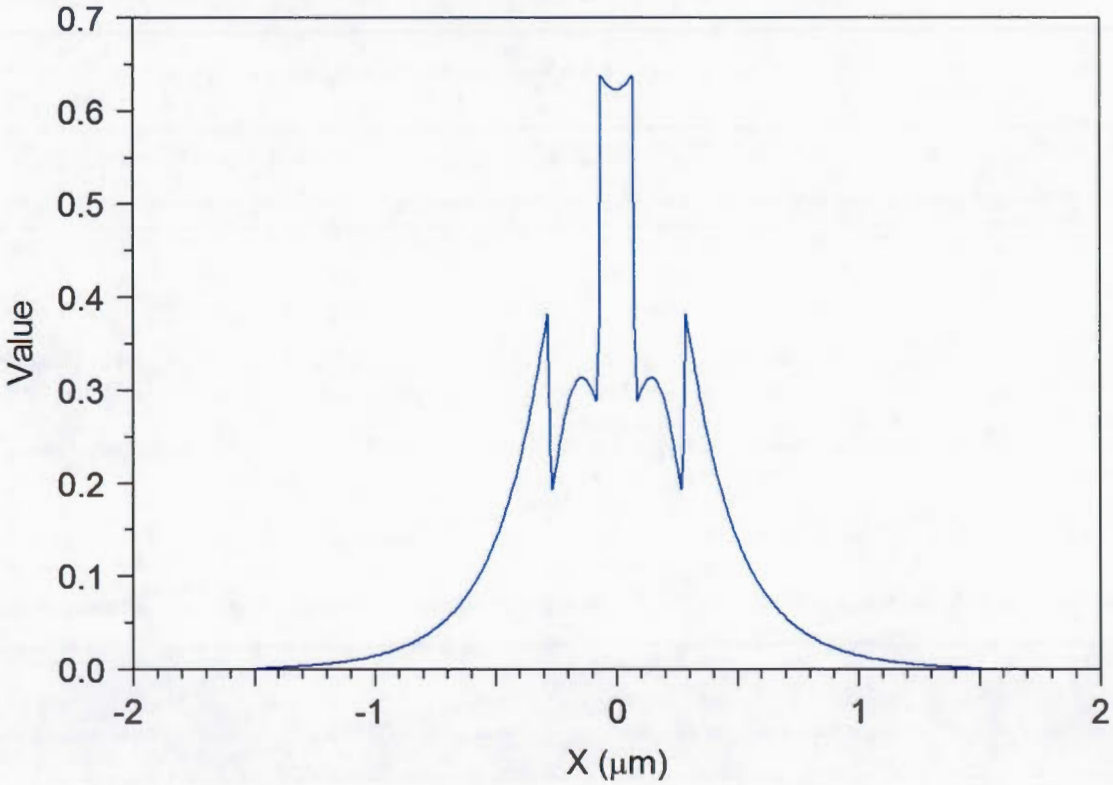

Figure IV.5: Horizontal cut of the E_x mode profile at Y=0

4.2 Effective Area of the Third-order Nonlinear Interaction

The effective area for nonlinear interaction A_{eff}, is an important measure in waveguides since the level of light interaction with the nonlinear material can be controlled by the waveguide geometry. The calculation of the effective area is based on the modal field. By considering the relation $\gamma \propto \chi^{(3)} / n^2 A_{eff}$, we understand that for a given third-order nonlinear susceptibility $\chi^{(3)}$, the nonlinear effects can be larger

if we have a smaller A_{eff}. The nonlinear susceptibility is a function of the materials that make up the cross-section of the waveguide.

In the slot waveguide structure, the total cross-section of the waveguide is D_{total} which comprises D_{Core}, D_{Sub} and D_{Cover} (see Fig. 4.1). A strong nonlinear interaction area exists inside the slot region covered with a nonlinear material because of the large electrical resulting from the high confinement of the fundamental quasi-TE mode. Thus, to calculate the nonlinear effective area, one needs to determine the region occupied by the mode in the cover domain, D_{cover}, where the cladding nonlinear material is located (see Fig. 4.1). Therefore, for the cladding nonlinearity, the interaction domain is $D_{inter} = D_{cover}$ and the linear refractive index of the nonlinear material in the D_{inter} is considered as n_{CV}. The effective area for the slot waveguide can be written as (Koos et al., 2007):

$$A_{eff} = \frac{Z_0^2}{n_{CV}^2} \frac{\left| \iint_{D_{tot}} \mathrm{Re}\{\boldsymbol{E}(x,y) \times \boldsymbol{H}^*(x,y).e_z dx\, dy\} \right|^2}{\iint_{D_{inter}} |\boldsymbol{E}(x,y)|^4\, dx\, dy} \qquad (4.1)$$

where $Z_0=\sqrt{\mu_0/\varepsilon_0}=377\ \Omega$ is the free-space wave impedance, and e_z is a unit vector pointing in positive z-direction. The modal fields $\boldsymbol{E}(x,y)$ and $\boldsymbol{H}(x,y)$ are classified by TE and TM mode. The electric and magnetic fields of the fundamental waveguide modes are calculated by using Beam Prop Method (BPM) simulations performed with RSoft, as described in the previous section.

To demonstrate the impact of the slot waveguide geometry and of the cladding material refractive index, the effective nonlinear interaction area A_{eff} was calculated with MATLAB for slot width in the range $110\ \mathrm{nm} < w_s < 140\ \mathrm{nm}$ and a nonlinear cladding material refractive index varying from $1 < n_{cover} < 3$. The results are presented in Fig. 4.9. For the lower cladding refractive indices, only a small part of the electromagnetic field is guided in the high index core material; therefore, the field enhancement increases and as it can be seen from Fig. 4.6, the effective area decreases. For a slot width of $w_s = 140$ nm with crystal violet as the nonlinear cover

material, which corresponds to one of the waveguide configuration on the test sample, the effective area is $A_{eff} = 0.321\ \mu m^2$.

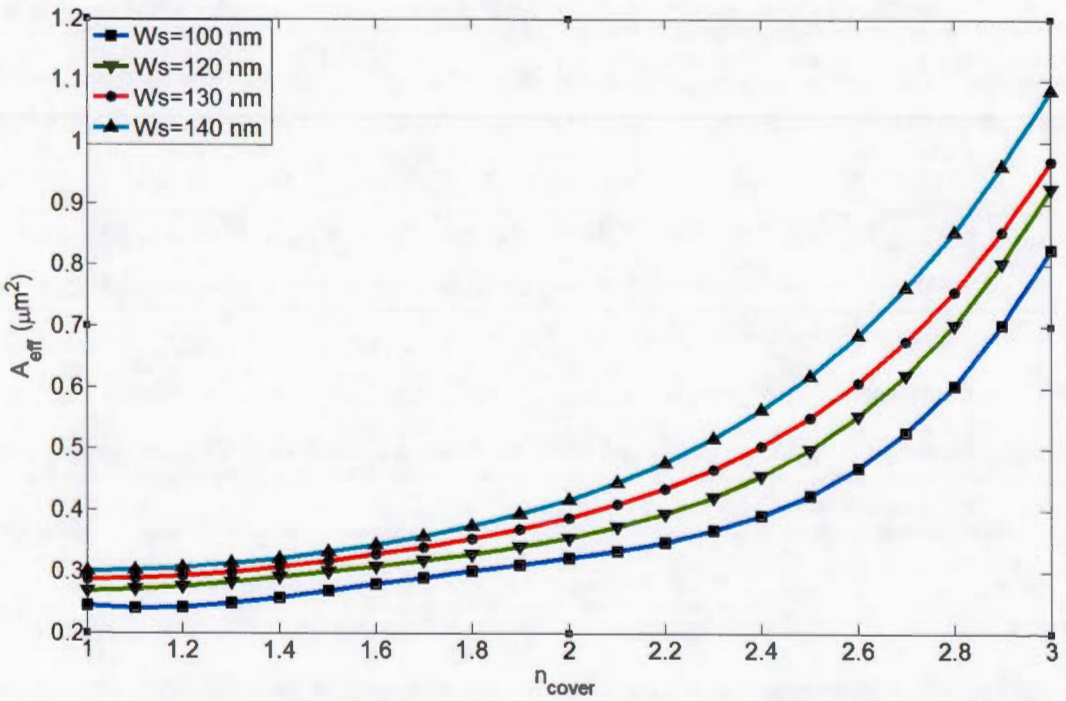

Figure IV.6: Effective area A_{eff} for various slot widths 100 nm<w_s<140 nm as a function of the cladding refractive index.

4.3 Dispersion and Phase-matching Condition

By using finite difference methods to compute the quasi-TE mode effective index as a function of wavelength, the group velocity dispersion (GVD) of the slot waveguides can be modeled by:

$$D = \frac{d\beta_1}{d\lambda} = -\frac{2\pi c}{\lambda^2}\beta_2 = -\frac{\lambda}{c}\frac{d^2 n_{eff}}{d\lambda^2} \qquad (4.2)$$

However, the precision of calculations depends on the grid size and the computational window. Therefore, a convergence study was performed to determine stable and accurate computation conditions. The final details of the calculations are as follows: computation window size is 3000 nm in the x and y direction and the grid sizes are

dx=10 nm and dy=11 nm. The results are presented in Fig. 4.7 for the range from λ=1.5 μm to λ=1.6 μm for different slot widths.

At a wavelength of λ=1.55 μm for crystal violet with a refractive index n_{CV}=1.51, the dispersion is found to be D=-3031 ps/(km nm).

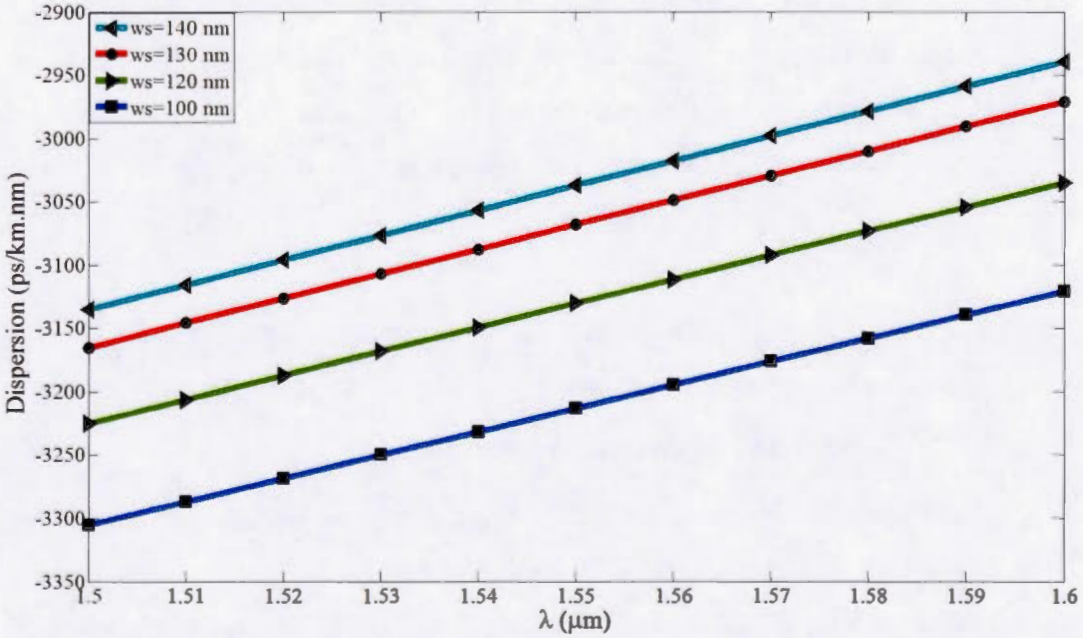

Figure IV.7: Simulated GVD for the TE mode as a function of wavelength for w_s=140 nm

Phase matching in FWM process is a critical requirement as discussed in the beginning of this section. The effects of dispersion must be considered as a critical parameter when evaluating the nonlinear characteristics of slot waveguides. However, the phase matching condition can be optimized by engineering of the dispersion properties of waveguides.

Dispersion engineering of SOI-based slot waveguides has been studied by Zheng, Iqbal and Liu (2008) at λ=1550 nm and the results demonstrate the dependence of the dispersion on the slot waveguide geometries, including the slot width and the filling material used in the slots. Thus, it is possible to improve the efficiency of nonlinear processes, such as FWM, in slot waveguides by engineering their dispersion. Ideally, for FWM the dispersion should be near to zero at the pump wavelength. The benefits

of this have been demonstrated with channel silicon waveguides, which through dispersion engineering have achieved broadband parametric gain and wavelength conversion (Lau *et al.*, 2011). As can be seen from Fig. 4.7, there are significant improvements possible with regards to the dispersion profile of the waveguides considered in this study. Nevertheless, this optimization is not straight forward since modifying the geometry of slot waveguides can also have a significant impact on their effective area, as illustrated in Fig. 4.6. Therefore, for this initial demonstration, the emphasis was put on slot waveguide geometries with a small effective area that were compatible with the fabrication process.

4.4 Nonlinear Parameters of Crystal Violet

4.4.1 Third Order Nonlinear Susceptibility

The third order nonlinear susceptibility of crystal violet was reported by measuring third-harmonic generation (THG) for fundamental wavelengths within the range 1100 nm< λ <1800 nm (Ramos-Ortiz et al., 2007). The nonlinear susceptibility of the crystal violet, which demonstrate the multidirectional charge transfer within its octupolar structure (three-fold symmetry), is in the order of $\chi^{(3)}=10^{-12}$ esu.

The third order nonlinear susceptibility $\chi^{(3)}$ for a polymer film doped with 10 wt. % of crystal violet is shown in Fig. 4.8 (Ramos-Ortiz *et al.*, 2007). At a wavelength of λ=1550 nm, the third order nonlinear susceptibility of crystal violet with a refractive index n_{CV}=1.51 is $\chi^{(3)}=4.7\times10^{-12}$ esu. These values were used in the FWM simulations described below.

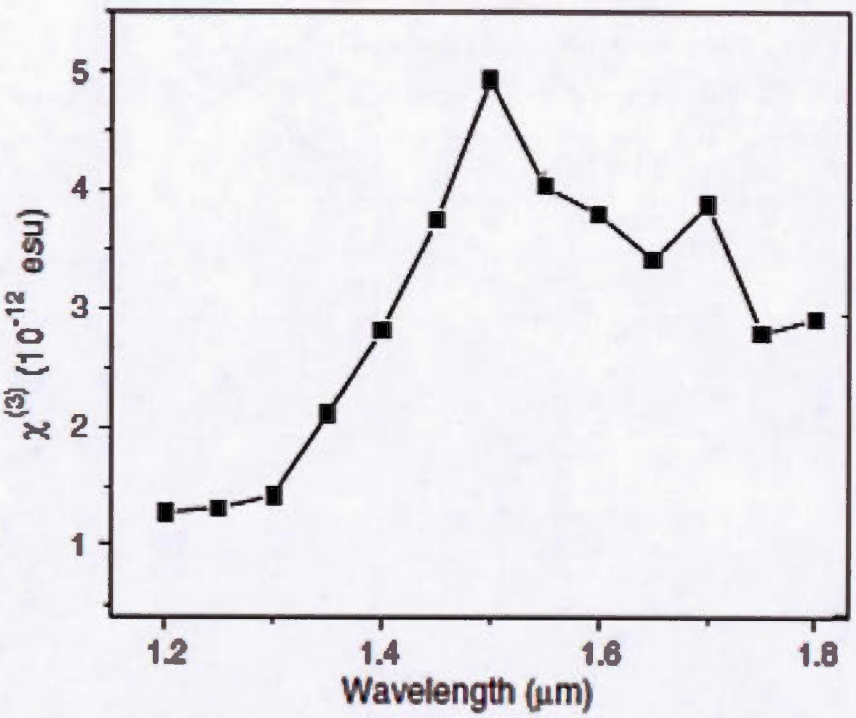

Figure IV.8: Third order nonlinear susceptibility for a polymer film doped with 10 wt. % crystal violet as a function of wavelength (adapted from Ramos-Ortiz *et al.*, 2007)

4.4.2 Nonlinear Waveguide Parameter

As discussed in section 2.2.1, in waveguides, the nonlinear parameter γ presents the intensity of the third-order nonlinear interaction:

$$\gamma = \frac{2\pi n_2}{\lambda_p \, A_{eff}} \tag{4.3}$$

The nonlinear refractive index of crystal violet n_2 (m^2/W), can be found by using the following equation (Okamoto, 2010 ; Tkach *et. al.*, 1995):

$$n_2[m^2/W] = \frac{480\pi^2\chi^{(3)}[\text{esu}]}{cn^2} \tag{4.4}$$

All calculations were performed at the telecommunication wavelength of λ_p =1550 nm. The dimensions and parameters for crystal violet used with a slot

width of w_s=140 are summarized in Table 4.2. Furthermore, the nonlinear parameter as a function of slot width w_s is presented in Table 4.3.

Table 4-2: Summary of material parameters and nonlinear coefficients for crystal violet

Rib width	w_r	200 nm
Slot width	w_s	140 nm
Rib height	h	220 nm
Length	L	1000 μm
Refractive index	n_{CV}	1.51
Propagation loss	α	3.0 dB/cm
Slot waveguide dispersion	D	-3031 ps/(km nm)
Nonlinear effective mode area	A_{eff}	0.321 μm^2
Nonlinear susceptibility	$\chi^{(3)}$	4.7×10^{-12} esu (Ramos-Ortiz *et al.*, 2007)
Nonlinear refractive index	n_2	$3.26 \times 10^{-17} m^2/W$

Table 4-3: Nonlinear parameter and nonlinear effective area for different slot widths

Slot Width w_s (nm)	Nonlinear Effective Mode Area A_{eff} (μm^2)	Nonlinear Parameter $\gamma (Wm)^{-1}$
100	0.279	473
120	0.301	438
130	0.319	414
140	0.335	394

The large nonlinear parameter calculated for crystal violet is due to the chromophore units attached to the backbone and it is approximately four times larger than that of silicon waveguide, which is 100 $(Wm)^{-1}$ (Vallaitis, 2014). Moreover, the nonlinear

parameter values obtained here are higher than for all the other devices reported in section 2.4, except for PTS.

4.5 FWM-based Wavelength Conversion

In the FWM process, to convert a signal that carries information to an idler wave, a continuous-wave (CW) pump is preferable since there is no synchronisation requirement between the pump and the signal as is the case with burst mode pumps. The coupled differential equations that model the FWM process were presented in section 2.3.2. There are various methods to model FWM wavelength conversion (Foster et al., 2007) but in this thesis, the most common approach is applied, which is solving the coupled differential equations numerically. In this case it was performed using a MATLAB script. Moreover, in the DFWM process the energy of two pump photons is converted and one signal photon and one idler photon are generated. The idler photon receives the information of the signal photon in this process. The wavelength conversion efficiency defined as the ratio of output idler power (P_{idler}^{out}) to output signal power (P_{signal}^{in}) can be written as:

$$\eta_{CE} = \frac{P_{idler}^{out}}{P_{signal}^{in}} \tag{4.5}$$

Therefore, the conversion efficiency as a function of idler wavelength can be numerically calculated by integrating the coupled-mode equations of FWM presented in section 2.3.2. A MATLAB script adapted from Ryan K.W. Lau (Lau et al., 2011) that solves the coupled-mode equations is used in this work.

In our DFWM model, the two-photon absorption (TPA) and self-phase modulation (SPM)/cross-phase modulation (XPM)-induced frequency mismatch are considered as limiting factors. The slot waveguide parameters used in the simulations are summarized in Table 4.2. To calculate the conversion efficiency, the pump wavelength is set at 1550 nm with an input pump power of 100 mW and the signal is continuously tuned from 1550 to 1565 nm for each waveguide. The theoretical

conversion efficiency as a function of idler wavelength for different slot width is shown in Figure 4.9. The peak conversion efficiency is approximately -12 dB for a slot waveguide filled with crystal violet with a slot width of w_s=100 nm. Moreover, these results show that within the range considered here, the slot width has little impact on the conversion efficiency and the achievable bandwidth. However, using the larger slot is preferable to implement the waveguides since it is easier to fill it with the nonlinear material.

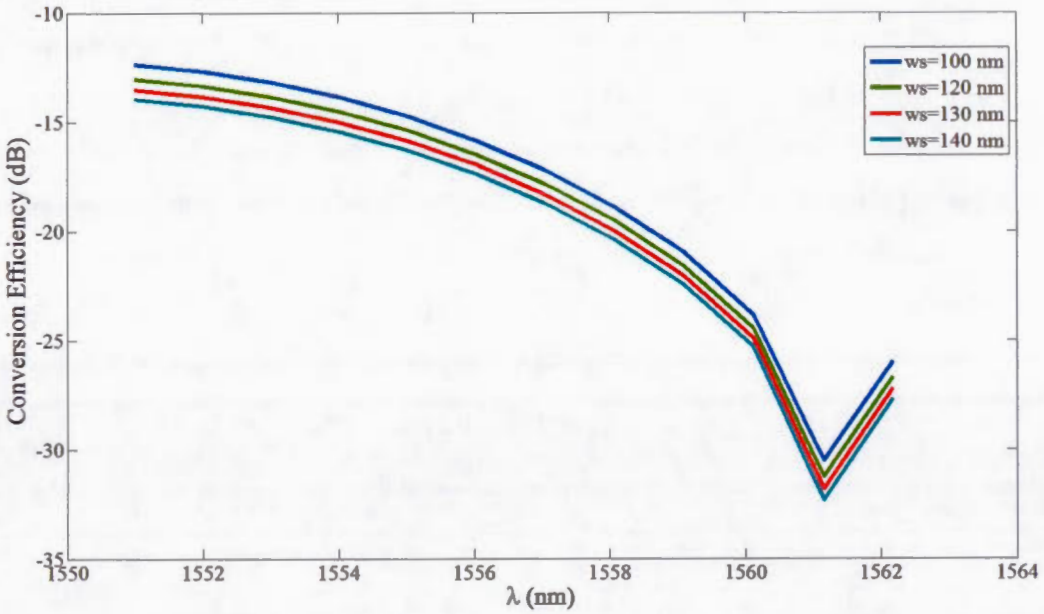

Figure 4.9: Theoretical conversion efficiency as a function of idler wavelength for slot waveguides filled with crystal violet 10 wt. % for slot widths 100 nm< w_s< 140 nm

The conversion efficiency of slot waveguides (shown in Fig. 4.9) is compared with the one of a silicon waveguide with a height and width of h=200 nm and w=500 nm, respectively. As it is shown in Fig. 4.10, the conversion efficiency of silicon waveguides with the same simulation parameters is approximately -18 dB, which is lower than that of slot waveguides with the nonlinear chromophores due to the large two-photon absorption coefficient of silicon. However, it should be mentioned that

silicon has a larger bandwidth than slot waveguides because of its dispersion properties.

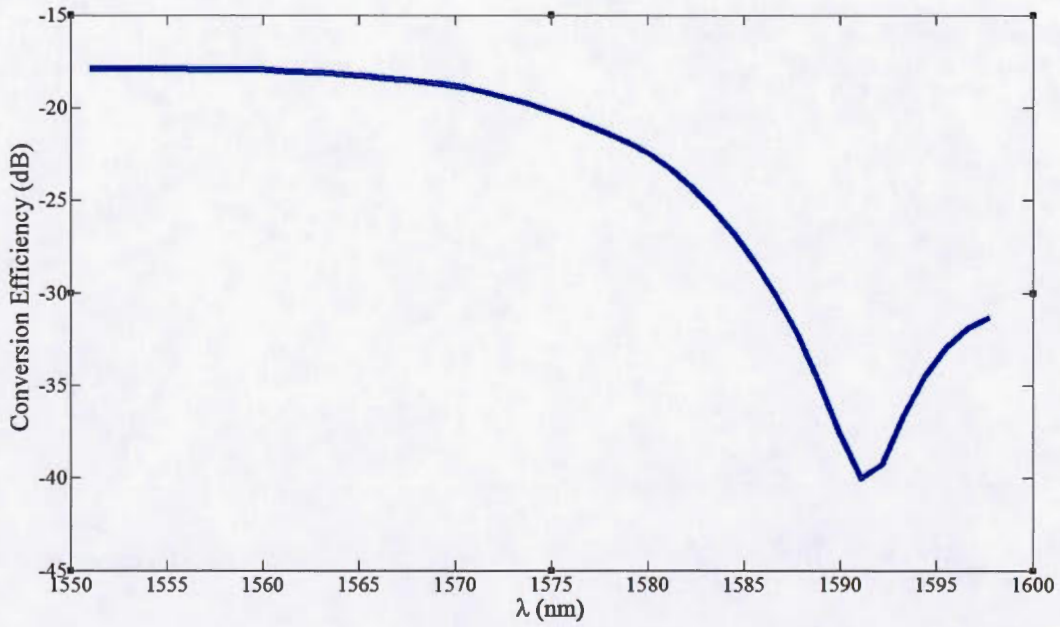

Figure 4.10: Theoretical conversion efficiency as a function of idler wavelength for a silicon channel waveguide

Moreover, the impact of increasing the pump power on the conversion efficiency of slot and silicon waveguides is studied. As shown in Fig. 4.11 and Fig. 4.12, when the pump power reach P_{in}=300 mW, the conversion efficiency of slot waveguides increases to 0 dB but for silicon it saturates at around -10 dB because of its large two-photon absorption coefficient. Thus, slot waveguides are more efficient at higher pump power than silicon channel waveguide.

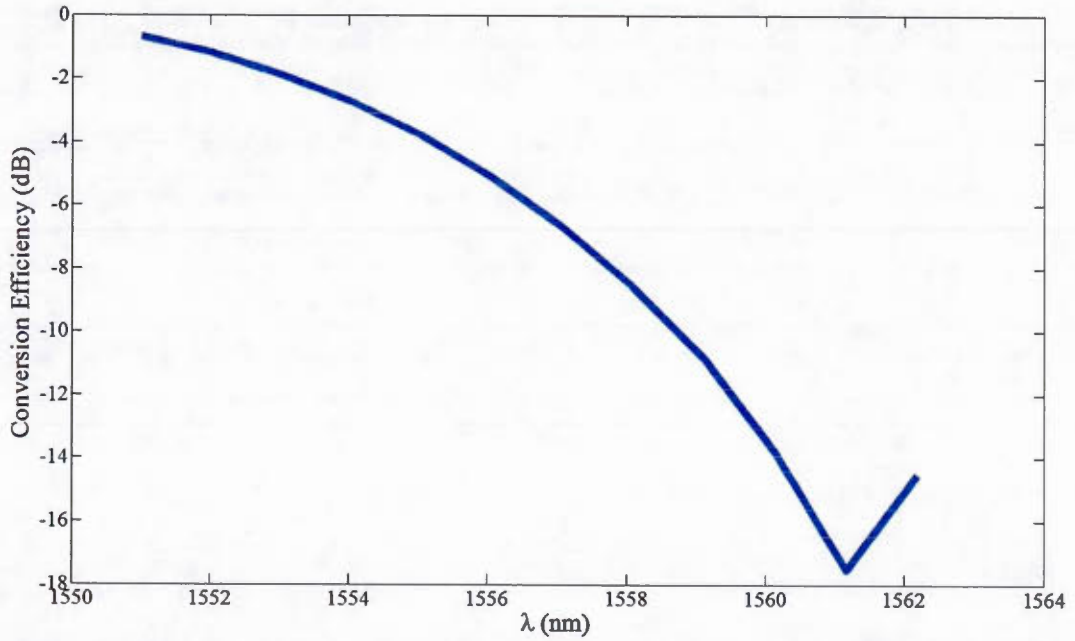

Figure 4.11: Theoretical conversion efficiency as a function of idler wavelength for slot waveguides with an input power of P_{in}=300 mW

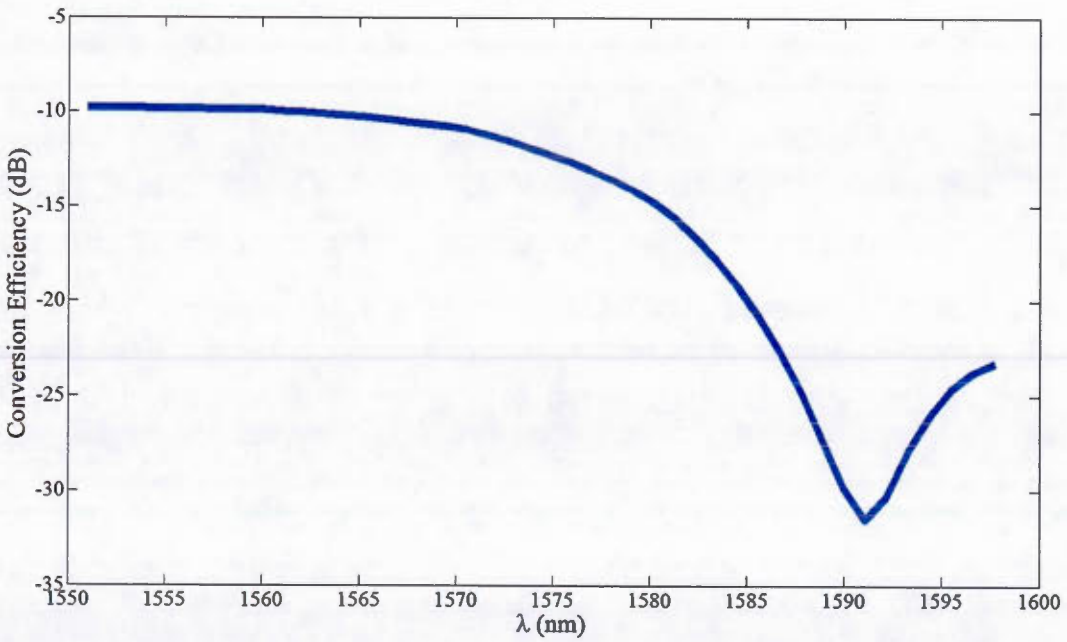

Figure 4.12: Theoretical conversion efficiency as a function of idler wavelength for silicon waveguide with an input power of P_{in}=300 mW

CHAPTER V

EXPERIMENTAL SETUP AND MEASUREMENTS

In this chapter, the experimental setup and corresponding results for linear loss measurements in a slot waveguide structure filled with crystal violet are discussed. Furthermore, the FWM-based wavelength conversion experiment is shown in details.

5.1 Experimental Setup and Measurements

As mentioned in section 3.2, grating couplers are used to couple light from a single-mode fiber into photonic integrated circuits as illustrated in Fig. 5.1.

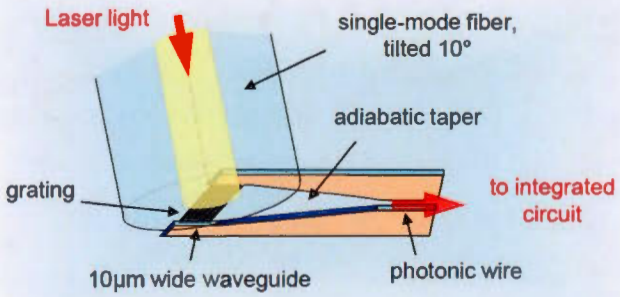

Figure 5.1: Schematic of a grating coupler used to couple light into a photonic integrated circuit (adapted from (Pello, 2014))

A standard setup is configured to measure the propagation loss of light coupled into the waveguides with grating couplers (see Fig. 5.2). Each element of this setup has a specific function that is described below:

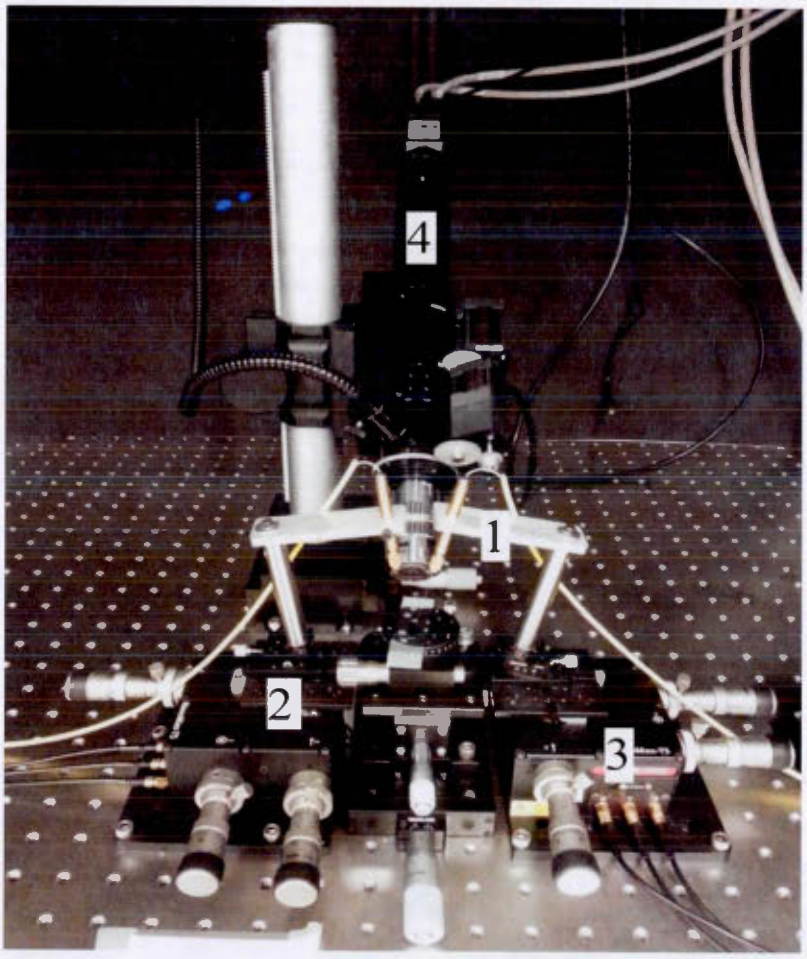

Figure 5.2: Loss measurement setup

1. **Fiber chuck holders**

   Fiber chucks maintain the fiber and the tips of the fibers are fixed at an angle of 10° with respect to the sample normal during the measurements. Fiber chuck holders were designed and fabricated to hold the fiber chucks while the other ends of fibers are connected to a source that can be a tunable laser, or an erbium-doped fiber amplifier (EDFA)) or to a detector such as a power-meter, or an optical spectrum analyzer (OSA).

2. **Goniometers**

   In order to adjust the fiber chuck holders to the optimum coupling angle, they are mounted on goniometers set to obtain an angle of ~10° between the fiber and the direction normal to the sample surface.

3. **Micropositioners**

   The fiber chuck holders are fixed on 3-axis micropositioners to precisely adjust their position.

4. **Alignment visible camera**

   A camera operating at visible wavelengths is placed at ~45° with respect to the sample surface to align the fibers relative to the on-chip grating couplers. To distinguish one waveguide from the others and position accurately the fibers with respect to the grating coupler, the resolution of the camera should be high. The camera used in this setup is connected to a 50× microscope objective using a tube of ~10 cm in length. After this initial visual alignment, the received power is maximized by fine tuning the position of the in and out-coupling fibers with the micropositionners.

5. **Polarization controller (not shown)**

   In order to control the polarization state of the input light, which needs to match the fundamental TE mode in the slot waveguide since it is the only polarization propagation through the device, a polarization controller is necessary between the fiber holder and the laser.

5.1.1 Propagation Loss Measurements

The propagation loss of the fabricated waveguides was obtained by performing measurements on similar waveguides of different length, which correspond to block A, B and C described in chapter 3. This is equivalent to the cutback method in which the output power P_1 of a waveguide of length L_1 is measured, and then the output

power P_2 for a different length L_2 is obtained. From this, the propagation loss can be evaluated with (Reed et Knights, 2004):

$$\alpha = \ln \frac{P_2/P_1}{L_1 - L_2} \tag{5.1}$$

The insertion loss $\alpha_{insertion}$ corresponds to $\alpha_{insertion} = \alpha_{coupling} + \alpha_{propagation}$ if all these losses are specified in a logarithmic scale. The measurement results are presented after the discussion on the cladding materials used.

In this work different solutions were used to achieve the lowest loss. First, 5 wt. % PMMA with a refractive index n=1.49 was used. The refractive index of PMMA is slightly lower than that of crystal violet, which means that a little bit more of the mode will be confined in the slots as demonstrated by the effective area simulations presented in Fig. 4.6. All the solutions were prepared with two different solvents: chlorobenzene and chloroform. The initial solvent was chlorobenzene but as explained in chapter 3 the solubility of crystal violet was limited in this case. Thus, we changed to chloroform to solve that issue. For the crystal violet solutions, different concentrations were deposited on the sample to perform the measurements but because of the opaqueness of the higher concentrations only 1 wt. % crystal violet and 5 wt. % PMMA dissolved in chloroform were used for the loss measurements. The dark color of the other concentration made the alignment of the coupling fibers impossible.

Therefore, the samples for which the losses were measured had the following cover materials:

- 5 wt. % PMMA dissolved in chlorobenzene,
- 5 wt. % PMMA dissolved in chloroform,
- 1 wt. % crystal violet and 5 wt. % PMMA dissolved in chloroform.

Figure 5.3 shows an example of data points and of the fitted line for a slot width of w_s=140 nm with a cladding of 5 wt. % PMMA dissolved in chlorobenzene. The measured insertion losses are for an input power of P_{in}=6.3 dBm. The three different

lengths of waveguides on the sample chip are exactly 3.726 mm, 9.369 mm, and 12.396 mm.

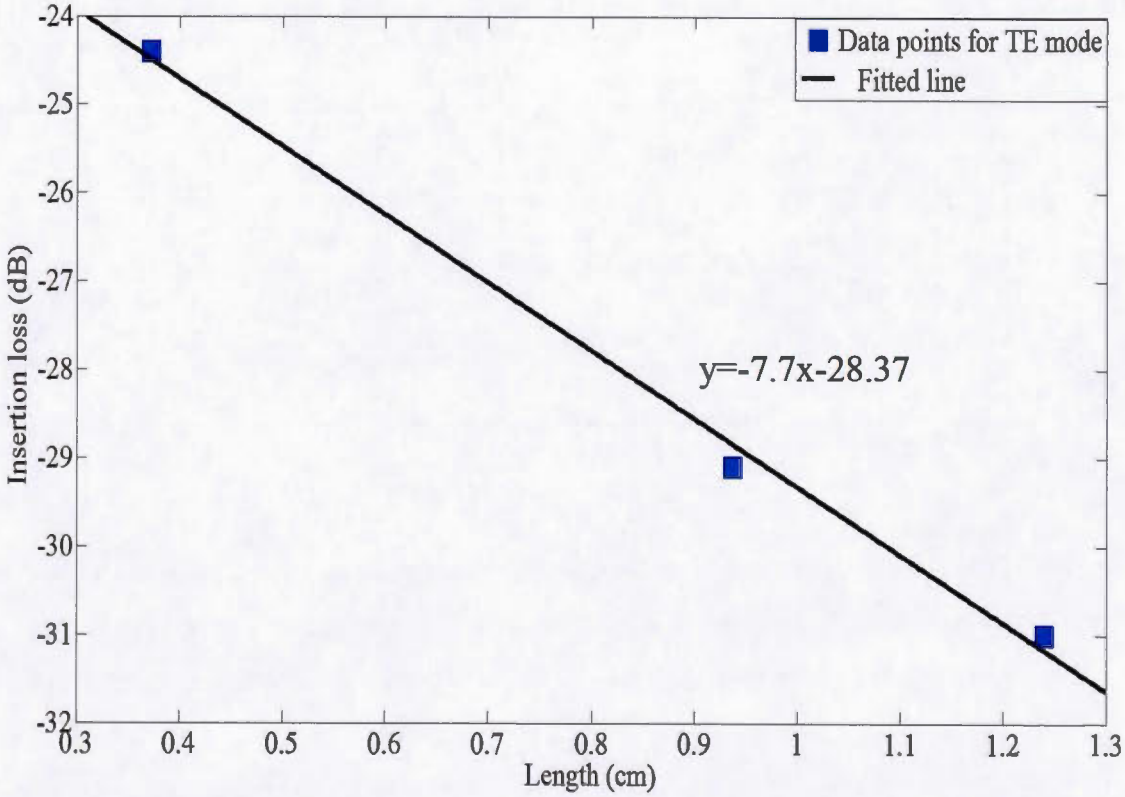

Figure 5.3: Measurement of the insertion loss for the fundamental TE mode for slot waveguides with a slot width of w_s=140 nm and cladded with 5 wt% PMMA dissolved in chlorobenzene.

Fiber alignments were performed to optimize the input and output power and then the losses were measured for various waveguide geometries and lengths. The propagation loss and insertion loss measurements results are presented Table 5.1 in for waveguides cladded with 5 wt. % PMMA dissolved in chlorobenzene. The value presented for the coupling loss is the total coupling loss. It should be divided by two to obtain the value per side.

Table 5-1: Measurements of insertion losses, propagation losses and coupling losses for waveguides filled with PMMA 5 wt. % dissolved in chlorobenzene

Waveguide	Propagation Loss (dB/cm)	Coupling Loss (dB)	Insertion Loss (dB)
A-100	12.9	15.0	27.9
A-130	8.8	20.5	29.3
A-140	7.7	20.7	28.4
Y-100	13.3	12.3	25.7

The lowest linear loss in this set of slot waveguide structures with this cover material is measured for a slot width of 140 nm and is ~7.7 dB/cm. The high losses of these waveguides in comparison to strip waveguides can be explained by the much higher level of interaction between the silicon sidewalls and the optical field. Indeed, in a strip waveguide the optical energy is concentrated in the middle of the core, away from the core/cladding interface. This is not the case in slot waveguides where light is confined between two very close interfaces. As a result, the light a slot waveguide is more affected by the roughness of the sidewalls, which results is losses through scattering. Moreover, the layout of the samples made it impossible to distinguish between certain causes of losses. For instance, the losses due to transition from strip to slot waveguide could not be measured. Since we expect this loss to be constant across waveguides of different lengths, it should be associated with the coupling losses. On the other hand, the different length of waveguides also had different number of bends. Thus, if any extra losses were induced by bending the waveguides, it is included in the propagation loss results. The bends were purposefully made with large radii (over 150 μm) in order to minimize bending losses. However, after

fabrication it was discovered that the slot width is not constant inside the bends, it tends to become larger, and this could have induced extra losses. Nevertheless, as explained in the discussion below our results compare favorably with those reported in literature and therefore we expect the impact of these width variations to be minimal.

Few measurements were successful with the waveguides having a slot width of 120 nm, especially those with adiabatic transition region. Since the waveguides with the smaller slot of 100 nm worked, this indicates that there was an issue with the layout of the 120 nm slots.

Next, the loss measurements were performed on slot waveguides filled with PMMA 5 wt. % dissolved in chloroform. As shown in Table 5.2, the lowest loss measured is ~6.5 dB/cm again for the slot of a 140 nm which has a lower propagation and insertion loss than that of PMMA 5 wt. % with chlorobenzene. Therefore, in addition to improve solubility, chloroform also provides better insertion losses. This is most likely due to a better filling of the slot and the grating couplers topology during the cladding deposition.

Table 5-2: Measurements of insertion losses, propagation losses and coupling losses for waveguides filled with PMMA 5 wt. % dissolved in chloroform

Waveguide	Propagation loss (dB/cm)	Coupling Loss (dB)	Insertion loss (dB)
A-100	7.52	9.9	17.5
A-130	9.5	6.6	16.1
A-140	6.5	9.3	15.8
Y-100	8.4	7.9	16.4
Y-120	7.6	8.6	16.2

Finally, crystal violet solutions dissolved in chloroform with concentrations ranging from 1 wt. % to 30 wt. % were prepared for the loss measurement experiments. Due to the opaque color of crystal violet, after deposition the fiber alignment becomes very difficult with the visible camera. Thus, the lowest concentration of crystal violet, 1 wt. %, was deposited on the sample and loss measurements were performed (see Table 5.3).

Table 5-3: Measurements of insertion losses, propagation losses and coupling losses for waveguides filled with crystal violet 1 wt. % dissolved in chloroform

Waveguide	Propagation loss (dB/cm)	Coupling Loss (dB)	Insertion loss (dB)
A-100	15.8	14.1	29.9
A-130	12.6	14.7	27.3
A-140	11.9	14.3	26.2
Y-100	14.0	12.1	26.1
Y-120	13.1	14.7	27.8

In this work, slot waveguides with crystal violet as the cladding material are studied for the first time and results show that the waveguide with the widest slot has the lowest loss. Nonetheless, the high loss in these waveguides is due to the deposition process of crystal violet into the slot waveguides. To minimize the loss, the solution concentrations and spin coating parameters such as spin speed, ramp and thickness have been varied. By using a profilometer, the thickness of 1 wt. % crystal violet and 5 wt. % PMMA in chloroform were measured to be 1.4 μm and 2.4 μm, respectively. This shows that the addition of only a small amount of crystal violet can have a tremendous impact on the solution viscosity. This increase in viscosity makes

the deposition of crystal violet inside slot waveguides challenging and can lead to very high losses if voids are present in the slot.

Based on the nonlinear parameter values reported for a solution with 10 % wt. crystal violet (see section 4.4.1), the expected conversion efficiency in slot waveguides with slot width of w_s= 140 nm and the experimentally measured propagation losses of α=11.9 dB/cm were simulated with an input power of P_{in}= 6.3 dBm and are presented in Fig. 5.4. The maximum expected conversion efficiency is only around -23 dB for this high concentration, which explains the results described in section 5.2 below.

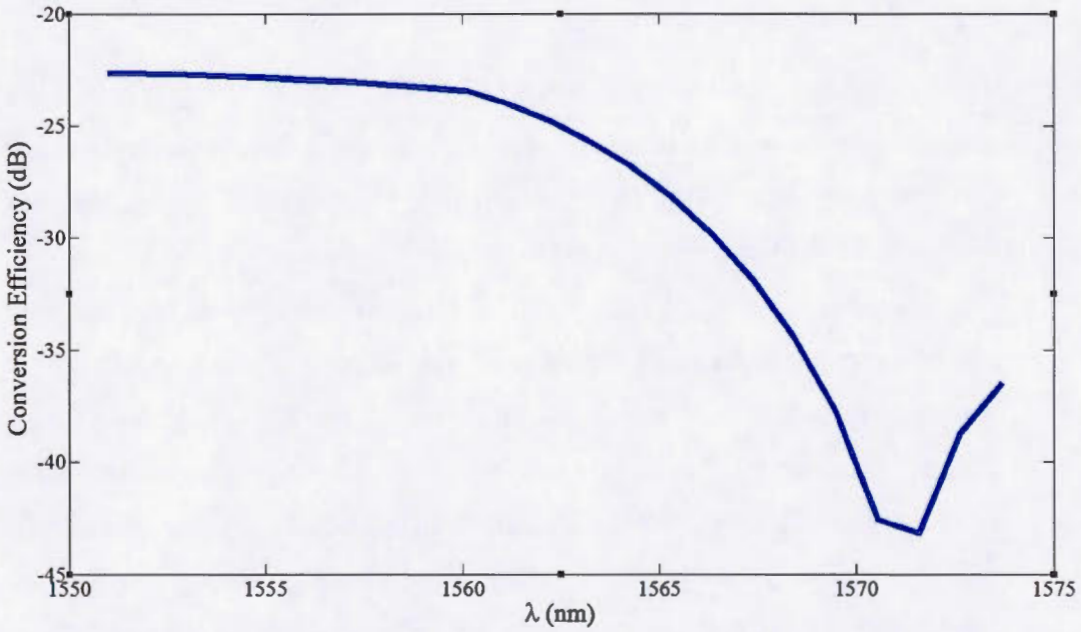

Figure 5.4: Expected conversion efficiency for slot waveguide with slot width of w_s= 140 nm filled with 1 wt. % crystal violet

Nevertheless, this work appears to be heading in the right direction to enable the efficient integration of crystal violet with silicon slot waveguides. The choice of chloroform as solvent for PMMA has produced hybrid organic/silicon devices that compare advantageously with the results reported in the literature. To the best of our knowledge, the lowest loss measured in SOI slot waveguides is ~5 dB/cm (Säynätjoki *et al.*, 2011) for waveguides with a 166 nm slot filled with aluminum

oxide (Al_2O_3). This is higher that our best results with PMMA diluted in chloroform, which 6.5 dB/cm, and it was obtained with a larger slot and an inorganic material. Thus, the slot waveguides filled with PMMA diluted in chloroform can be considered as low loss structures for this type of waveguides. As for the integration of the nonlinear chromophores, in future work different concentrations of crystal violet with appropriate deposition methods need to be investigated to achieve lower losses.

5.2 FWM-based Wavelength Conversion Experiment

5.2.1 Experimental Setup for Four-wave mixing

The experimental setup used to measure DFWM is shown in Fig. 5.5. It includes two tunable external cavity lasers (ECLs) used as the pump and signal sources and a high power erbium doped fiber amplifier (EDFA) that is placed next to the pump laser (ECL1) to amplify it as much as possible.

The pump laser (ECL1), which is set at a wavelength of 1550 nm and can be amplified to output up to 33dBm is combined with the signal laser (ECL1), which is working at 1549 nm and has an output power of 16 dBm, through a 90/10 coupler. Before the coupler the pump and signal lasers output goes through different polarization controllers (PCs) to adjust their polarization state to match that of the slot waveguide. The output of the coupler is launched into the slot waveguides with a single mode fiber (SMF), as shown in Fig. 5.2. Finally, the output is fiber-coupled back to a SMF and it is analyzed with an optical spectrum analyzer (OSA).

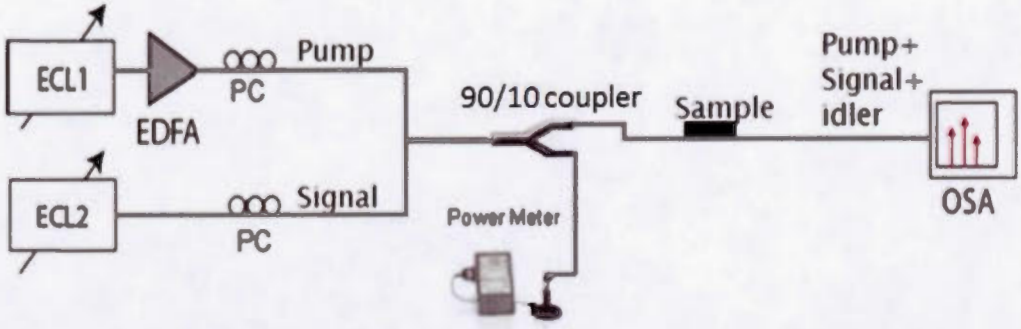

Figure 5.5: FWM experimental setup: ECL: External cavity laser; EDFA: Erbium doped fiber amplifier; PC: Polarization controller; OSA: Optical spectrum analyzer; PM: Power meter (adapted from (Brès *et al.*, 2011))

The input power of the pump is varied from 5.5 dBm to 33 dBm but despite this high input power it was not sufficient to observe the generation of an idler wave. This is probably due to the combination of high insertion loss and of the small fraction of crystal violet (only 1% wt.) that was possible to successfully integrate in the slot waveguides. Indeed, the previous nonlinear characterisations of crystal violet were performed with thin films having concentration ranging from 10 to 30% wt (Ramos-Ortiz et al., 2004). Therefore, increasing the crystal violet concentration of the cladding while improving its integration with the slot waveguides are clear goals for the future of this work. In light of the small initial concentration that was demonstrated here this may seem challenging. However, with slot waveguide the concentration required to achieve nonlinear effects should be smaller than in thin films because of the high level of interaction that the slot confinement provides with the optical field. Moreover, the use of PMMA diluted in chloroform appears as a promising solution to achieve low losses.

CHAPTER VI

CONCLUSION

In this thesis, the integration of highly nonlinear crystal violet chromophore with silicon waveguides having a slot geometry was studied for the first time. This work laid the foundation for the development of a novel category of highly nonlinear hybrid silicon devices that exploit the unique design and optimization opportunities made possible by chromophores relying on multi-charge transfer transitions. The first simulation study of the four-wave mixing conversion efficiency in slot waveguides filled with crystal violet was done. Furthermore, the characterisation of the propagation losses of slot waveguides filled with PMMA diluted in chloroform was performed. Moreover, a deposition process for crystal violet chromophores in a PMMA host on silicon slot waveguides was elaborated. Finally, the challenges of using crystal violet in the cladding of silicon photonic devices were described, and the experimental characterisation of the propagation losses of slot waveguides filled with a polymer containing crystal violet chromophores was completed.

The nonlinear optical chromophores considered in this study have shown great values of second-order hyperpolarizability due to their high polarized π-electron backbone and multidirectional charge transfer transitions. Therefore, this type of chromophore could potentially be used to realize innovative and high performance devices.

The main goal of this thesis was to evaluate and demonstrate slot waveguide structures filled with crystal violet that would provide a strong light confinement within the slot region, minimize the effective mode area, and enhance the nonlinear parameter for wavelength conversion.

The slot waveguide structure has been studied with the Rsoft software by using a full-vectorial finite-difference mode solver [i.e. Beam Propagation Method (BPM)] to simulate the Eigenmodes of the waveguides and to obtain the transverse electric field distribution of the quasi-TE mode. Furthermore, the dispersion profile, the effective mode area of slot waveguide structure, and the nonlinear parameter were estimated by using a MATLAB script.

The effective mode area and the nonlinear parameter of a slot waveguide with a slot width of w_r=140 nm for the TE-mode were calculated to be A_{eff}=0.321 μm^2 and $\gamma = 394\ (Wm)^{-1}$, respectively. The nonlinear parameter estimated was approximately four times larger than that of silicon, which is 100 $(Wm)^{-1}$.

Thus, the calculated nonlinear parameters (A_{eff}, $\chi^{(3)}$, n_2, γ) were used to numerically solve the coupled-mode theory equations of FWM and by employing these parameters in a MATLAB script, the conversion efficiency as a function of idler wavelength was found.

The waveguides were fabricated at CMC Microsystems and IMEC. The dimensions such as height, width and slot width of a slot waveguide were chosen to be 220 nm, 240nm and 100-140 nm, respectively, to assure a minimum effective area and a large nonlinear parameter. In addition, the device had a 2.5 μm layer of crystal violet as a cover material. The 1 wt. to 30 wt. % crystal violet solutions were prepared by dissolving 30 mg of crystal violet per percent in a 5 wt.% PMMA (i.e.150 mg of PMMA in chloroform).

The linear loss coefficient of the slot waveguide cladded with crystal violet and PMMA was determined using waveguides of different length. The estimated linear propagation loss for the 140 nm-wide slot waveguide structure filled with for 1 wt. % crystal violet at 1550 nm for TE-mode was found to be 11$\pm$0.5 dB/cm. The impact of losses on the conversion efficiency was simulated and it shows that at high pump powers, slot waveguides are more efficient than silicon channel waveguides because

of the large TPA coefficient of silicon. Thus, slot waveguides can potentially achieve high conversion efficiency for third-order nonlinear effects such as four-wave mixing.

This work made it possible to clearly identify the challenges of integrating crystal violet chromophores with silicon slot waveguides. There is an important trade-off between the chromophore concentration and the cladding solution viscosity that remains to be optimized to build efficient nonlinear devices. Nevertheless, the experimental results obtained here indicate that chloroform is a suitable solvent for that task. Moreover, using waveguides with larger slot appears to be beneficial since, according to simulations, the impact on the FWM conversion efficiency is minimal despite the increase in effective area. It also simplifies fabrication and leads to waveguides with lower propagation losses. Finally, to be able to characterise polymer with a high concentration of crystal violet, it will be necessary to develop a technique to keep track of the grating coupler locations or to avoid depositing the polymer on them because its dark colour makes it impossible to see the features under the cladding. Also, it will be useful to study more in depth the slot filling and uniformity of the deposition, use other chromophores and try different methods of deposition to determine the possible causes of high losses with this material.

REFERENCES

Agrawal, G.P. 2013a. *Nonlinear Fiber Optics*: Academic Press p. En ligne. <http://books.google.ca/books?id=xNvw-GDVn84C>.

Agrawal, Govind (2013b). Nonlinear Fiber Optics (5th Edition), Elsevier En ligne. <http://app.knovel.com/hotlink/toc/id:kpNFOE0003/nonlinear-fiber-optics/nonlinear-fiber-optics>.

Agrawal, Govind P. 2012. *Fiber-optic communication systems*: John Wiley & Sons p.

Al-Kadhemy, MFH, et WH Abaas. 2012. «Absorption spectrum of Crystal Violet in Chloroform solution and doped PMMA thin films». Atti della Fondazione Giorgio Ronchi, vol. 67, no 3, p. 359.

Almeida, Vilson R, Qianfan Xu, Carlos A Barrios et Michal Lipson. 2004. «Guiding and confining light in void nanostructure». *Optics Letters*, vol. 29, no 11, p. 1209-1211.

Anderson, P Andrew, Bradley S Schmidt et Michal Lipson. 2006. «High confinement in silicon slot waveguides with sharp bends». *Optics Express*, vol. 14, no 20, p. 9197-9202.

Asobe, M, I Yokohama, T Kaino, S Tomaru et T Kurihara. 1995. «Nonlinear absorption and refraction in an organic dye functionalized main chain polymer waveguide in the 1.5 μm wavelength region». *Applied Physics Letters*, vol. 67, no 7, p. 891-893.

Assefa, Solomon, Fengnian Xia et Yurii A Vlasov. 2010. «Reinventing germanium avalanche photodetector for nanophotonic on-chip optical interconnects». *Nature*, vol. 464, no 7285, p. 80-84.

Baehr-Jones, Tom, Michael Hochberg, Chris Walker et Axel Scherer. 2005a. «High-Q optical resonators in silicon-on-insulator-based slot waveguides». *Applied Physics Letters*, vol. 86, no 8, p. 081101.

Baehr-Jones, Tom, Michael Hochberg, Guangxi Wang, Rhys Lawson, Yi Liao, Philip A Sullivan, L Dalton, AK-Y Jen et Axel Scherer. 2005b. «Optical modulation

and detection in slotted silicon waveguides». *Optics Express*, vol. 13, no 14, p. 5216-5226.

Baehr-Jones, Tom, Boyan Penkov, Jingqing Huang, Phil Sullivan, Joshua Davies, Jocelyn Takayesu, Jingdong Luo, Tae-Dong Kim, Larry Dalton et Alex Jen. 2008. «Nonlinear polymer-clad silicon slot waveguide modulator with a half wave voltage of 0.25 V». *Applied Physics Letters*, vol. 92, no 16, p. 163303.

Barrios, Carlos Angulo, et Michal Lipson. 2005. «Electrically driven silicon resonant light emitting device based on slot-waveguide». *Optics Express*, vol. 13, no 25, p. 10092-10101.

Bhowmik, Achintya K, et Mrinal Thakur. 2001. «Self-phase modulation in polydiacetylene single crystal measured at 720-1064nm». *Optics Letters*, vol. 26, no 12, p. 902-904.

Bogaerts, Wim, Pieter Dumon, Dries Van Thourhout et Roel Baets. 2007. «Low-loss, low-cross-talk crossings for silicon-on-insulator nanophotonic waveguides». *Optics Letters*, vol. 32, no 19, p. 2801-2803. En ligne. <http://ol.osa.org/abstract.cfm?URI=ol-32-19-2801>.

Bosshard, Christian, Rolf Spreiter, Peter Günter, Rik R Trkwinski, Martin Schreiber et François Diederich. 1996. «Structure-property relationships in nonlinear optical tetraethynylethenes». *Advanced Materials*, vol. 8, no 3, p. 231-234.

Brès, Camille-Sophie, Sanja Zlatanovic, Andreas O. J. Wiberg et Stojan Radic. 2011. «Continuous-wave four-wave mixing in cm-long Chalcogenide microstructured fiber». *Optics Express*, vol. 19, no 26, p. B621-B627. En ligne. <http://www.opticsexpress.org/abstract.cfm?URI=oe-19-26-B621>.

Boyd, Robert W. 2003. *Nonlinear optics*: Academic press p.

Cardinal, T., Richardson, K. A., Shim, H., Schulte, A., Beatty, R., Le Foulgoc, K., ... & Villeneuve, A. (1999). Non-linear optical properties of chalcogenide glasses in the system As–S–Se. Journal of Non-Crystalline Solids, 256, 353-360.

Celler, GK, et Sorin Cristoloveanu. 2003. «Frontiers of silicon-on-insulator». Journal of Applied Physics, vol. 93, no 9, p. 4955-4978.

Diament, Paul. 1990. *Wave transmission and fiber optics*: Macmillan publishing company p.

Dinu, M, F Quochi et H Garcia. 2003. «Third-order nonlinearities in silicon at telecom wavelengths». *Applied Physics Letters*, vol. 82, no 18, p. 2954-2956.

Dong, Po, Ning-Ning Feng, Dazeng Feng, Wei Qian, Hong Liang, Daniel C Lee, BJ Luff, T Banwell, A Agarwal et P Toliver. 2010. «GHz-bandwidth optical filters based on high-order silicon ring resonators». *Optics Express*, vol. 18, no 23, p. 23784-23789.

Duguay, MA, Y Kokubun, TL Koch et Loren Pfeiffer. 1986. «Antiresonant reflecting optical waveguides in SiO2-Si multilayer structures». *Applied Physics Letters*, vol. 49, no 1, p. 13-15.

Dulkeith, Eric, Yurii A Vlasov, Xiaogang Chen, Nicolae C Panoiu et Richard M Osgood Jr. 2006. «Self-phase-modulation in submicron silicon-on-insulator photonic wires». *Optics Express*, vol. 14, no 12, p. 5524-5534.

Fallahkhair, Arman B, Kai S Li et Thomas E Murphy. 2008. «Vector finite difference modesolver for anisotropic dielectric waveguides». *Journal of lightwave technology*, vol. 26, no 11, p. 1423-1431.

Fang, Alexander W, Hyundai Park, Oded Cohen, Richard Jones, Mario J Paniccia et John E Bowers. 2006. «Electrically pumped hybrid AlGaInAs-silicon evanescent laser». *Optics Express*, vol. 14, no 20, p. 9203-9210.

Feit, MD, et JA Fleck Jr. 1978. «Light propagation in graded-index optical fibers». *Applied Optics*, vol. 17, no 24, p. 3990-3998.

Flytzanis, Ch. 1975. «Quantum electronics: A treatise». *Rabin, H*, p. 9.

Foresi, JS, B Little, G Steinmeyer, E Thoen, S Chu, H Haus, E Ippen, L Kimerling et W Greene. 1997. *Si/SiO 2 Micro-Ring Resonator Optical Add/Drop Filters: Conference on Lasers and Electro-Optics*. Optical Society of America, CPD22 p.

Foster, M, K Moll et Alexander Gaeta. 2004. «Optimal waveguide dimensions for nonlinear interactions». *Optics Express*, vol. 12, no 13, p. 2880-2887.

Foster, Mark A, Amy C Turner, Reza Salem, Michal Lipson et Alexander L Gaeta. 2007. «Broad-band continuous-wave parametric wavelength conversion in silicon nanowaveguides». *Optics Express*, vol. 15, no 20, p. 12949-12958.

Foster, Mark A, Amy C Turner, Jay E Sharping, Bradley S Schmidt, Michal Lipson et Alexander L Gaeta. 2006. «Broad-band optical parametric gain on a silicon photonic chip». *Nature*, vol. 441, no 7096, p. 960-963.

Friberg, Stephen R, et Peter W Smith. 1987. «Nonlinear optical glasses for ultrafast optical switches». *Quantum Electronics, IEEE Journal of*, vol. 23, no 12, p. 2089-2094.

Fukuda, Hiroshi, Koji Yamada, Tetsufumi Shoji, Mitsutoshi Takahashi, Tai Tsuchizawa, Toshifumi Watanabe, Jun-ichi Takahashi et Sei-ichi Itabashi. 2005. «Four-wave mixing in silicon wire waveguides». *Optics Express*, vol. 13, no 12, p. 4629-4637.

Gambling, WA. 2000. «The rise and rise of optical fibers». *Selected Topics in Quantum Electronics, IEEE Journal of*, vol. 6, no 6, p. 1084-1093.

Gao, SM, ZQ Li et XZ Zhang. 2010. «Power-attenuated optimization for four-wave mixing-based wavelength conversion in silicon nanowire waveguides». *Journal of Electromagnetic waves and Applications*, vol. 24, no 8-9, p. 1255-1265.

Gregory, Peter. 2012. *High-technology applications of organic colorants*: Springer Science & Business Media p.

Greve, Daniel R, Steen B Schougaard, Tommy Geisler, Jan C Petersen et Thomas Biørnholm. 1997. «Large third-order nonlinear optical response from molecules with effective multidirectional charge-transfer transitions: New design of third-order nonlinear chromophores». *Advanced Materials*, vol. 9, no 14, p. 1113-1116.

Gubler, Ulrich. 2000. «Third-order nonlinear optical effects in organic materials». Diss. Naturwissenschaften ETH Zürich, Nr. 13605, 2000.

Gubler, Ulrich, et Christian Bosshard. 2002. «Molecular design for third-order nonlinear optics». In *Polymers for Photonics Applications I*, p. 123-191: Springer.

Hansryd, Jonas, Peter A Andrekson, Mathias Westlund, Jie Li et Per-Olof Hedekvist. 2002. «Fiber-based optical parametric amplifiers and their applications». *Selected Topics in Quantum Electronics, IEEE Journal of*, vol. 8, no 3, p. 506-520.

Harbold, JM, FÖ Ilday, FW Wise, JS Sanghera, VQ Nguyen, LB Shaw et ID Aggarwal. 2002. «Highly nonlinear As-S-Se glasses for all-optical switching». *Optics Letters*, vol. 27, no 2, p. 119-121.

Huang, Xinyu, et William J. Brittain. 2001. «Synthesis and Characterization of PMMA Nanocomposites by Suspension and Emulsion Polymerization». *Macromolecules*, vol. 34, no 10, p. 3255-3260. En ligne. <http://dx.doi.org/10.1021/ma001670s>.

Igarashi, Koji, et Kazuro Kikuchi. 2008. «Optical signal processing by phase modulation and subsequent spectral filtering aiming at applications to ultrafast optical communication systems». Selected Topics in Quantum Electronics, IEEE Journal of, vol. 14, no 3, p. 551-565.

IMEC (2012). *imec SiPhotonics Standard Passives (PSV) Technology Handbook.* Ghent University.: Pieter Dumon

Jamid, Husain A. 2002. «Multilayer ARROW channel waveguide for evanescent field enhancement in low-index media». *Applied Optics*, vol. 41, no 7, p. 1385-1390.

Kaino, Toshikuni. 2000. «Waveguide fabrication using organic nonlinear optical materials». *Journal of Optics A: Pure and Applied Optics*, vol. 2, no 4, p. R1.

Kajzar, F, J Messier, DS Chemla et J Zyss. 1987. «Nonlinear Optical Properties of Organic Molecules and Crystals». *Vol. II, edited by Chemla, DS, and Zyss, J.,(Academic, Orlando, Fl)*, p. 51-83.

Kang, Yimin, Han-Din Liu, Mike Morse, Mario J Paniccia, Moshe Zadka, Stas Litski, Gadi Sarid, Alexandre Pauchard, Ying-Hao Kuo et Hui-Wen Chen. 2009. «Monolithic germanium/silicon avalanche photodiodes with 340 GHz gain–bandwidth product». *Nature Photonics*, vol. 3, no 1, p. 59-63.

Kim, Dug Y, Michael Sundheimer, Akira Otomo, George Stegeman, Winfried HG Horsthuis et Guus R Möhlmann. 1993. «Third order nonlinearity of 4-dialkylamino-4'nitro-stilbene waveguides at 1319 nm». *Applied Physics Letters*, vol. 63, no 3, p. 290-292.

Koos, C, L Jacome, C Poulton, J Leuthold et W Freude. 2007. «Nonlinear silicon-on-insulator waveguides for all-optical signal processing». *Optics Express*, vol. 15, no 10, p. 5976-5990.

Koos, Christian. 2007. *Nanophotonic Devices for Linear and Nonlinear Optical Signal Processing*: p.

Kuo, Ying-Hao, Haisheng Rong, Vanessa Sih, Shengbo Xu, Mario Paniccia et Oded Cohen. 2006. «Demonstration of wavelength conversion at 40 Gb/s data rate in silicon waveguides». *Optics Express*, vol. 14, no 24, p. 11721-11726.

Kuwata-Gonokami, M, S Ozawa, RH Jordan, A Dodabalapur, HE Katz, ML Schilling et RE Slusher. 1995. «Polymer microdisk and microring lasers». *Optics Letters*, vol. 20, no 20, p. 2093-2095.

Kuzyk, Mark G., Kenneth D. Singer et George I. Stegeman. 2013. «Theory of Molecular Nonlinear Optics». *Advances in Optics and Photonics*, vol. 5, no 1, p. 4-82. En ligne. <http://aop.osa.org/abstract.cfm?URI=aop-5-1-4>.

Lau, Ryan KW, Michaël Ménard, Yoshitomo Okawachi, Mark A Foster, Amy C Turner-Foster, Reza Salem, Michal Lipson et Alexander L Gaeta. 2011. «Continuous-wave mid-infrared frequency conversion in silicon nanowaveguides». *Optics Letters*, vol. 36, no 7, p. 1263-1265.

Lawrence, BL, M Cha, JU Kang, W Toruellas, G Stegeman, G Baker, J Meth et S Etemad. 1994. «Large purely refractive nonlinear index of single crystal P-toluene sulphonate (PTS) at 1600 nm». *Electronics Letters*, vol. 30, no 5, p. 447-448.

Leong, Julie Y, Periklis Petropoulos, Symeon Asimakis, Heike Ebendorff-Heidepriem, Roger C Moore, Ken Frampton, Vittoria Finazzi, Xian Feng, Jonathan H Price et Tanya M Monro. 2005. *A Lead Silicate Holey Fiber with γ= 1820 W-1 km-1 at 1550 nm*: *Optical Fiber Communication Conference*. Optical Society of America, PDP22 p.

Leuthold, J., W. Freude, J. M. Brosi, R. Baets, P. Dumon, I. Biaggio, M. L. Scimeca, F. Diederich, B. Frank et C. Koos. 2009. «Silicon Organic Hybrid Technology—A Platform for Practical Nonlinear Optics». *Proceedings of the IEEE*, vol. 97, no 7, p. 1304-1316.

Leuthold, J., C. Koos et W. Freude. 2010. «Nonlinear silicon photonics». *Nature Photonics*, vol. 4, no 8, p. 535-544. In *a9h*. EBSCOhost. En ligne. <http://search.ebscohost.com/login.aspx?direct=true&db=a9h&AN=52556313&lang=fr&site=ehost-live>

Levy, Jacob. 2011. «Integrated nonlinear optics in silicon nitride waveguides and resonators».

Li, Zhihong, et Guifang Li. 2006. «Ultrahigh-speed reconfigurable logic gates based on four-wave mixing in a semiconductor optical amplifier». *Ieee Photonics Technology Letters*, vol. 18, no 9/12, p. 1341.

Lin, Qiang, Jidong Zhang, Philippe M Fauchet et Govind P Agrawal. 2006. «Ultrabroadband parametric generation and wavelength conversion in silicon waveguides». *Optics Express*, vol. 14, no 11, p. 4786-4799.

Lipson, Michal. 2005. «Guiding, modulating, and emitting light on silicon-challenges and opportunities». *Journal of lightwave technology*, vol. 23, no 12, p. 4222.

Little, BE, ST Chu, PP Absil, JV Hryniewicz, FG Johnson, F Seiferth, D Gill, V Van, O King et M Trakalo. 2004. «Very high-order microring resonator filters for WDM applications». *Photonics Technology Letters, IEEE*, vol. 16, no 10, p. 2263-2265.

Liu, Jia-Ming. 2005. Photonic devices: Cambridge University Press p.

Liu, Qiang, Shiming Gao, Zhiqiang Li, Yanqiao Xie et Sailing He. 2011. «Dispersion engineering of a silicon-nanocrystal-based slot waveguide for broadband wavelength conversion». *Applied Optics*, vol. 50, no 9, p. 1260-1265.

Luther-Davies, Barry, et Marek Samoc. 1997. «Third-order nonlinear optical organic materials for photonic switching». *Current Opinion in Solid State and Materials Science*, vol. 2, no 2, p. 213-219. En ligne. <http://www.sciencedirect.com/science/article/pii/S135902869780068X>.

Marcuse, Dietrich. 1972. «Light transmission optics».

Masanovic, Milan L, Vikrant Lal, Joseph A Summers, Jonathon S Barton, Erik J Skogen, Lavanya G Rau, Larry A Coldren et Daniel J Blumenthal. 2005. «Widely tunable monolithically integrated all-optical wavelength converters in InP». *Journal of lightwave technology*, vol. 23, no 3, p. 1350.

Moore, Gordon E. 1998. «Cramming more components onto integrated circuits». *Proceedings of the IEEE*, vol. 86, no 1, p. 82-85.

Okamoto, Katsunari. 2010. *Fundamentals of optical waveguides*: Access Online via Elsevier p.

Ophir, Noam, Ryan KW Lau, Michaël Ménard, Reza Salem, Kishore Padmaraju, Yoshitomo Okawachi, Michal Lipson, Alexander L Gaeta et Keren Bergman.

2012b. «First demonstration of a 10-Gb/s RZ end-to-end four-wave-mixing based link at 1884 nm using silicon nanowaveguides». *Photonics Technology Letters, IEEE*, vol. 24, no 4, p. 276-278. En ligne. <http://ieeexplore.ieee.org.proxy.bibliotheques.uqam.ca:2048/ielx5/68/6133462/06084814.pdf?tp=&arnumber=6084814&isnumber=6133462>.

Ophir, N., R. K. W. Lau, M. Menard, X. Zhu, K. Padmaraju, Y. Okawachi, R. Salem, M. Lipson, A. L. Gaeta et K. Bergman. 2012a. «Wavelength conversion and unicast of 10-Gb/s data spanning up to 700 nm using a silicon nanowaveguide». *Optics Express*, vol. 20, no 6, p. 6488-6495. En ligne. <http://www.scopus.com/inward/record.url?eid=2-s2.0-84858980143&partnerID=40&md5=c00c78d6111c4c4fd6aadf50eb0a8e32>.

Park, Joon, et Roderic S Lakes. 2007. Biomaterials: an introduction: Springer Science & Business Media p.

Paschotta, R., October 2008,'two-photon absorption' in the Encyclopedia of Laser Physics and Technology, 1., Wiley-VCH, ISBN 978-3-527-40828-3

Pello, J Josselin. 2014. «Building up a membrane photonics platform in Indium phosphide». Eindhoven, Technische Universiteit Eindhoven. En ligne. <http://repository.tue.nl/770716>.

Preston, Kyle Jonathan. 2011. Deposited silicon photonics: Optical interconnect devices in polycrystalline silicon: p.

Radamson, Henry, et Lars Thylen. 2014. Monolithic Nanoscale Photonics-Electronics Integration in Silicon and Other Group IV Elements: Academic Press p.

Ramos-Ortiz, G., J. L. Maldonado, M. A. Meneses-Nava, O. Barbosa-García, M. Olmos et M. Cha. 2007. «Third-harmonic generation performance of organic polymer films doped with triphenylmethane derivative dyes». *Optical Materials*, vol. 29, no 6, p. 636-641. En ligne. <http://www.sciencedirect.com/science/article/pii/S0925346705004994>.

Reed, Graham T, et Andrew P Knights. 2004. *Silicon photonics: an introduction*: John Wiley & Sons p.

Reed, Graham T, G Mashanovich, FY Gardes et DJ Thomson. 2010. «Silicon optical modulators». *Nature Photonics*, vol. 4, no 8, p. 518-526.

Robinson, Jacob T, Long Chen et Michal Lipson. 2008. «On-chip gas detection in silicon optical microcavities». *Optics Express*, vol. 16, no 6, p. 4296-4301.

Rochford, K, Raymond Zanoni, George I Stegeman, W Krug, E Miao et MW Beranek. 1991. «Measurement of nonlinear refractive index and transmission in polydiacetylene waveguides at 1.319 μm». *Applied Physics Letters*, vol. 58, no 1, p. 13-15.

Säynätjoki, A, L Karvonen, T Alasaarela, X Tu, TY Liow, M Hiltunen, A Tervonen, GQ Lo et S Honkanen. 2011. «Low-loss silicon slot waveguides and couplers fabricated with optical lithography and atomic layer deposition». *Optics Express*, vol. 19, no 27, p. 26275-26282.

Scarmozzino, R, A Gopinath, R Pregla et S Helfert. 2000. «Numerical techniques for modeling guided-wave photonic devices». *Selected Topics in Quantum Electronics, IEEE Journal of*, vol. 6, no 1, p. 150-162.

Scarmozzino, Robert, et Richard M Osgood Jr. 1991. «Comparison of finite-difference and Fourier-transform solutions of the parabolic wave equation with emphasis on integrated-optics applications». *JOSA A*, vol. 8, no 5, p. 724-731.

Schmidt, Holger, Yin Dongliang et Aaron R Hawkins. 2003. *Integrated optical spectroscopy of low-index gases and liquids using ARROW waveguides: Integrated Photonics Research*. Optical Society of America, ITuC2 p.

Semaltianos, N. G. 2007. «Spin-coated PMMA films». *Microelectronics Journal*, vol. 38, no 6–7, p. 754-761. En ligne. <http://www.sciencedirect.com/science/article/pii/S0026269207000870>. Consulté le 2007/7//.

Sharping, Jay E, Marco Fiorentino, Ayodeji Coker, Prem Kumar et Robert S Windeler. 2001. «Four-wave mixing in microstructure fiber». *Optics Letters*, vol. 26, no 14, p. 1048-1050.

Shen, Yuen-Ron. 1984. «Principles of nonlinear optics».

Shettigar, Seetharam, G Umesh, K Chandrasekharan et Balakrishna Kalluraya. 2007. «Third order nonlinear optical properties and two photon absorption in newly synthesized phenyl sydnone doped polymer». *Synthetic metals*, vol. 157, no 2, p. 142-146.

Simos, C, L Rodriguez, Vladimir Skarka, X Nguyen Phu, N Errien, G Froyer, TP Nguyen, P Le Rendu et P Pirastesh. 2005. «Measurement of the third order

nonlinear properties of conjugated polymers embedded in porous silicon and silica». *physica status solidi (c)*, vol. 2, no 9, p. 3232-3236.

Soltani, Mohammad, Siva Yegnanarayanan et Ali Adibi. 2007. «Ultra-high Q planar silicon microdisk resonators for chip-scale silicon photonics». *Optics Express*, vol. 15, no 8, p. 4694-4704.

Stolen, Roger H, et John E Bjorkholm. 1982. «Parametric amplification and frequency conversion in optical fibers». *Quantum Electronics, IEEE Journal of*, vol. 18, no 7, p. 1062-1072.

Suhara, T., et H. Nishihara. 1986. «Integrated optics components and devices using periodic structures». *Quantum Electronics, IEEE Journal of*, vol. 22, no 6, p. 845-867.

Thakur, M, et DM Krol. 1990. «Demonstration of all-optical phase modulation in polydiacetylene waveguides». *Applied Physics Letters*, vol. 56, no 13, p. 1213-1215.

Tkach, RW, AR Chraplyvy, Fabrizio Forghieri, AH Gnauck et RM Derosier. 1995. «Four-photon mixing and high-speed WDM systems». *Lightwave Technology, Journal of*, vol. 13, no 5, p. 841-849.

Townsend, PD, GL Baker, NE Schlotter, CF Klausner et S Etemad. 1988. «Waveguiding in spun films of soluble polydiacetylenes». *Applied Physics Letters*, vol. 53, no 19, p. 1782-1784.

Tsang, HK, CS Wong, TK Liang, IE Day, SW Roberts, A Harpin, J Drake et M Asghari. 2002. «Optical dispersion, two-photon absorption and self-phase modulation in silicon waveguides at 1.5 μm wavelength». *Applied Physics Letters*, vol. 80, no 3, p. 416-418.

Vallaitis, Thomas. 2014. *Ultrafast nonlinear silicon waveguides and quantum dot semiconductor optical amplifiers*: KIT Scientific Publishing p.

Vallaitis, Thomas, Siegwart Bogatscher, Luca Alloatti, Pieter Dumon, Roel Baets, Michelle L. Scimeca, Ivan Biaggio, François Diederich, Christian Koos, Wolfgang Freude et Juerg Leuthold. 2009. «Optical properties of highly nonlinear silicon-organic hybrid (SOH) waveguide geometries». *Optics Express*, vol. 17, no 20, p. 17357-17368. En ligne. <http://www.opticsexpress.org/abstract.cfm?URI=oe-17-20-17357

<http://www.opticsinfobase.org/DirectPDFAccess/FA2DDA62-CA82-DA37-1DACB7B491195799_185934/oe-17-20-17357.pdf?da=1&id=185934&seq=0&mobile=no>.

Vlasov, Yurii. 2012. «Silicon CMOS-integrated nano-photonics for computer and data communications beyond 100G». *Communications Magazine, IEEE*, vol. 50, no 2, p. s67-s72.

Vlasov, Yurii A, Martin O'Boyle, Hendrik F Hamann et Sharee J McNab. 2005. «Active control of slow light on a chip with photonic crystal waveguides». *Nature*, vol. 438, no 7064, p. 65-69.

Wang, Jie, Chunyan Chen, Sarah M. Buck et Zhan Chen. 2001. «Molecular Chemical Structure on Poly(methyl methacrylate) (PMMA) Surface Studied by Sum Frequency Generation (SFG) Vibrational Spectroscopy». *The Journal of Physical Chemistry B*, vol. 105, no 48, p. 12118-12125. En ligne. <http://dx.doi.org/10.1021/jp013161d>.

Williams, David J. 1984. «Organic Polymeric and Non-Polymeric Materials with Large Optical Nonlinearities». *Angewandte Chemie International Edition in English*, vol. 23, no 9, p. 690-703.

Willner, Alan E, Omer Faruk Yilmaz, Jian Wang, Xiaoxia Wu, Antonella Bogoni, Lin Zhang et Scott R Nuccio. 2011. «Optically efficient nonlinear signal processing». Selected Topics in Quantum Electronics, IEEE Journal of, vol. 17, no 2, p. 320-332.

Xia, Fengnian, Mike Rooks, Lidija Sekaric et Yurii Vlasov. 2007. «Ultra-compact high order ring resonator filters using submicron silicon photonic wires for on-chip optical interconnects». *Optics Express*, vol. 15, no 19, p. 11934-11941.

Xu, Lin, Noam Ophir, Michael Menard, Ryan Kin Wah Lau, Amy C Turner-Foster, Mark A Foster, Michal Lipson, Alexander L Gaeta et Keren Bergman. 2011. «Simultaneous wavelength conversion of ASK and DPSK signals based on four-wave-mixing in dispersion engineered silicon waveguides». *Optics Express*, vol. 19, no 13, p. 12172-12179.

Xu, Qianfan, Vilson R Almeida, Roberto R Panepucci et Michal Lipson. 2004. «Experimental demonstration of guiding and confining light in nanometer-size low-refractive-index material». *Optics Letters*, vol. 29, no 14, p. 1626-1628.

Yamada, Hirohito, Masayuki Shirane, Tao Chu, Hiroyuki Yokoyama, Satomi Ishida et Yasuhiko Arakawa. 2005. «Nonlinear-optic silicon-nanowire waveguides». *Japanese journal of applied physics*, vol. 44, no 9R, p. 6541.

Yang, Allen HJ, Sean D Moore, Bradley S Schmidt, Matthew Klug, Michal Lipson et David Erickson. 2009. «Optical manipulation of nanoparticles and biomolecules in sub-wavelength slot waveguides». *Nature*, vol. 457, no 7225, p. 71-75.

Zhao, Ming-Tang, Bhanu P. Singh et Paras N. Prasad. 1988. «A systematic study of polarizability and microscopic third-order optical nonlinearity in thiophene oligomers». *Journal of Chemical Physics*, vol. 89, no 9, p. 5535. In *a9h*. EBSCOhost. En ligne. <http://search.ebscohost.com/login.aspx?direct=true&db=a9h&AN=7619216&lang=fr&site=ehost-live>.

Zheng, Zheng, Muddassir Iqbal et Jiansheng Liu. 2008. «Dispersion characteristics of SOI-based slot optical waveguides». *Optics Communications*, vol. 281, no 20, p. 5151-5155. En ligne. <http://www.sciencedirect.com/science/article/pii/S003040180800641X>.

Zyss, J, I Ledoux, M Bertault et E Toupet. 1991. «Dimethylaminocyanobiphenyl (DMACB): A new optimized molecular crystal for quadratic nonlinear optics in the visible». *Chemical physics*, vol. 150, no 1, p. 125-135.

Zyss, Joseph, Thai Chau Van, Christophe Dhenaut et Isabelle Ledoux. 1993. «Harmonic Rayleigh scattering from nonlinear octupolar molecular media: the case of crystal violet». *Chemical physics*, vol. 177, no 1, p. 281-296.